Aalto-yliopisto
Aalto-universitetet
Aalto University

Master's Degree in Energy Storage

DETECTION OF SECONDARY PHASE IN NMC811$(OH)_2$ PRECURSOR USING X-RAY POWDER DIFFRACTION AND RAMAN SPECTROSCOPY

ARJUN MURALIDHARAN

Master's Thesis
2023

Aalto-yliopisto
Aalto-universitetet
Aalto University

Author Muralidharan Arjun

Title of thesis Detection of secondary phase in NMC811$(OH)_2$ precursor using X-ray powder diffraction and Raman spectroscopy

Programme Double Degree Master's in Energy Storage

Major Energy Storage

Thesis supervisor Prof. Kallio Tanja

Thesis advisor Dr. Kong Xiangze

Collaborative partner Umicore Finland Oy

Date 18-Oct-2023 **Number of pages** 68 **Language** English

Abstract

Nowadays, the popularity of lithium-ion batteries (LIBs) has surged across various sectors, from consumer electronics to electric vehicles and even higher-capacity stationary energy storage. Among the different types of cathode active materials for LIBs, Ni-rich oxides, have gained prominence in LIBs technology due to their cost-effectiveness and high energy density. Various dopants for Ni-rich cathode materials further enhance their electrochemical performance. In this research work, an initial investigation is carried out to explore and approximate the potential for the dopant's detection when adding various compounds to the Ni-rich precursor.

This study employs the identification of the crystal structure of NMC811$(OH)_2$ precursor and precursor mixed with compounds was investigated using X-ray diffraction (XRD) and Raman spectroscopy. To investigate the precursor more in detail, *in-situ* high temperature XRD (*in-situ* HT-XRD) was utilized to study the phase transformations and crystallization processes of the precursor during temperature increasing from 25°C to 900°C in the air atmosphere. Then, four compounds were investigated (mixing with precursor), MoO_3, $Al(OH)_3$, $Zr(OH)_4$, and $Mg(OH)_2$. The preliminary XRD pattern supports the NMC811$(OH)_2$ precursor's strong crystallinity. The precursors *in-situ* HT-XRD analysis reveal the development of new crystallites from nickel (Ni), manganese (Mn), and cobalt (Co) hydroxides to oxides. When precursor mix with compounds, according to research findings from XRD, for MoO_3 and $Al(OH)_3$ case, the best secondary phase detection happens when a compound is added to the precursor at a concentration of roughly 1% by weight, giving information on the compound's doping potential. As for Raman, Ni, Mn, Co, and OH functional groups were found in the precursor. When precursor mixed with MoO_3 (1% by weight), Raman peaks were strong, evident, and matched the XRD findings. However, $Al(OH)_3$ had weak Raman signals, which cannot be detected when mixed with the precursor. For $Zr(OH)_4$ as it has an amorphous structure and the secondary peaks were not detectable by XRD; and $Mg(OH)_2$ XRD pattern match close to the precursor XRD, which is hard to be distinguished, so both $Mg(OH)_2$ and $Zr(OH)_4$ were not investigated further.

A detailed characterization by using XRD, *in-situ* HT-XRD, and Raman spectroscopy can offer possibilities for learning about Ni-rich precursors, complex chemical interactions, phase transformation, and secondary phase detection. The knowledge gained holds the potential to serve as a valuable guide for enhancing the development of future doping Ni-rich cathode materials for LIBs.

Keywords: NMC811$(OH)_2$ precursor, XRD, *In-situ* HT-XRD, Raman spectroscopy, Secondary phase.

Aalto-yliopisto
Aalto-universitetet
Aalto University

Table of Contents

Aalto-yliopisto
Aalto-universitetet
Aalto University

LIST OF FIGURES

LIST OF TABLES

Aalto-yliopisto
Aalto-universitetet
Aalto University

Acknowledgment

I would like to sincerely thank everyone who helped finish this thesis, which is titled "Detection of secondary phase in NMC811(OH)$_2$ precursor using X-ray powder diffraction and Raman spectroscopy”. I wish to sincerely thank Umicore, the global materials technology and recycling organization, for their excellent support and cooperation during this research effort. I am grateful for the opportunity to work for a reputable organization that has led the way in technological development in leading circular materials.

I would like to express my sincere gratitude to the advisors from Umicore for their unwavering guidance and support. Their expertise, valuable feedback, and willingness to share their knowledge have been instrumental in shaping the direction and focus of this research. I am indebted to them for their time, patience, and commitment to my academic and professional growth.

My appreciation also goes out to Aalto University faculty and staff, who have given me the supportive academic environment and tools I needed to do this research. Firstly, to Professor Kallio Tanja, who provided me with this great opportunity to do this master’s thesis in the Chemical Engineering department, I would like to express my gratitude for the advice and mentorship I received from my academic advisor Dr. Kong Xiangze whose knowledge, valuable input, and helpful criticisms through every step of work were crucial in determining the format and substance of this thesis. They have consistently inspired me throughout this journey with their everlasting support and confidence in my skills and knowledge. Additionally, a lot of credit must also go to all of the staff members and teammates who contributed their expertise and offered support not only for this project but also in other ways.

In addition, the experience I've had over the past two years would not have been possible without the ongoing encouragement and support I've gotten from my family and friends, who have sacrificed so much for me in order to give me the freedom to try new things and express myself.

Arjun Muralidharan

18-Oct-2023

Aalto-yliopisto
Aalto-universitetet
Aalto University

Abbreviation

LCO	$LiCoO_2$
LFP	$LiFePO_4$
LMO	$LiMnO_2$
NCA	$LiNi_{1-x-y}Co_xAl_yO_2$
NMC/L-NMC	$LiNi_{1-x-y}Co_xMn_yO_2$
L-NMC811	$LiNi_{0.8}Mn_{0.1}Co_{0.1}O_2$
Li-NMC-O_2	Lithium transition metal oxides
P-NMC811/NMC811 precursor	Precursor $Ni_{0.8}Mn_{0.1}Co_{0.1}(OH)_2$
OEM	Original equipment manufacturer
LIB	Lithium-ion battery
SSP	Shared socioeconomic pathways
XRD	X-ray powder diffraction
COD	Crystallographic open database
ICDD	International centre for diffraction data
EVs	Electric vehicles
SES	Stationary energy storage

1. Introduction

Modern technology relies heavily on batteries, which are essential for powering our devices. However, over time, these batteries degrade, leading to reduced energy storage capacity and efficiency. To meet the growing demand for longer lifespan and more efficient energy sources, it is crucial to develop batteries with significantly improved energy density and durability.

Batteries are classified into two main categories: primary batteries, which are disposable and offer a single discharge cycle; and secondary batteries, which can be recharged multiple times. Historically, primary batteries have been used to provide short-term, grid-independent power to portable devices. In contrast, secondary batteries, particularly those based on lithium-ion (Li^+ ion) technology with high nickel content, have gained prominence in recent years. These energy-dense secondary batteries have played a pivotal role in the acceptance in various automotive sectors due to improved performance and reduced reliance on critical elements like cobalt.

$LiNi_{0.8}Mn_{0.1}Co_{0.1}O_2$ (L-NMC811) cathode materials are distinguished among many battery choices because of their superior energy density and economical price. Nevertheless, it poses many difficulties like safety issues and durability that need to be resolved. In addition, compared to other cathode materials, the durability of L-NMC811 may be compromised when working at higher voltages. In industry and academy, the L-NMC811 cathode material usually synthesized from Ni-rich precursors.

Unfortunately, there is little information available about the testing and analysis of the $Ni_{0.8}Mn_{0.1}Co_{0.1}(OH)_2$ precursors (P-NMC811), specifically about its crystal structure, secondary phases, and imperfections, which would be affect the cathode materials' properties after their lithiation. P-NMC811 testing and investigation of its crystal structure, secondary phases, and defects are, nonetheless, areas where there is a noticeable lack of information.

On the other hand, the introduction of various compounds (dopants) into the positive electrode of the battery has proven to enhance the electrochemical performance of the LIBs. Currently, there are a plethora of studies including the dopants of Ti [1] [2], Al [3] [4], Zr [3], Mg [4] and W [5], Mo [6], and more. Therefore, in this research work an approximation to the doping is done by just mixing and incorporating compounds like MoO_3, $Al(OH)_3$, $Mg(OH)_2$ and $Zr(OH)_4$, into the Ni-rich precursor and detecting if there is any secondary phase. Using XRD and Raman spectroscopy at various percentages by weight of these compounds, intending to investigate the secondary phases detection limits and limitations of these instruments and also identify the secondary phases present in these compounds while mixed with precursor. The inclusion of dopants at different stages of cathode manufacture, such as during the precursor stage or at the lithiation stage, has been the subject of numerous studies to enhance the cycling performance of nickel-rich cathode materials. Therefore, this research may offer some information regarding the detection capacities of these equipment and the amount that may be added at various stages of positive electrode development. Besides, this research could help to promote the development of LIB technology by deepening the understanding of the structure and properties of the precursor, paving the way to enhanced performance, cost-effectiveness, stability, and reliability. Also, hoping that this research will help to clarify the complexity of cathode materials development and progress LIB technology as we pursue more effective, secure, and long-lasting energy storage solutions.

2. Literature review

Several research endeavours delving into the importance and necessity of energy storage for achieving extensive decarbonization tend to neglect the vital aspect of ensuring a balanced relationship between energy density and power output [7]. Battery storage systems can affect the whole system when we use different types of batteries and use different amounts of renewable energy for various applications. Battery voltage comes from the cathode and anode's electrochemical potential difference. Higher cathode potential and lower anode potential make for a higher voltage battery [8]. A battery's capacity and voltage are predicated on the type of active material employed in the cathode because the cathode is one of the key components that determine the overall performance and energy storage capabilities of a battery [9]. The identification and exploration of cost-effective substitutes for the cathode, involving novel materials, represents a crucial aspect of the deployment of electric vehicles (EVs) [10].

LIBs have emerged as a widely sought-after energy storage solution on account of their environmentally friendly nature, possessing a remarkable energy density and exceptional cycling proficiency [11]. The three most costly parts of a LIBs are the cathode, separator, and electrolyte [10]. Li^+ ion migrates during charge and returns during discharge, Li^+ ions movement enables the flow of electric current and the generation of electricity. This makes LIBs rechargeable [9]. Rechargeable batteries are essential for electrochemical energy storage through electrodes [11]. The first commercial LIB, $LiCoO_2$ (LCO), has good cation ordering, structural stability, and high Li^+ ion and electrical conductivity, but suffers from oxygen gas release at high voltage and only delivers half of its theoretical capacity [12]. To meet various energy storage needs, safe cathode cycling at high voltages is crucial [12], as LCO has a faster discharge rate for high loads [13]. However, progress is hindered by a lack of understanding of how material characteristics affect reactivity among the current LIBs technology. Because of its 200 mAh g^{-1} specific capacity and low Co content, the Ni-rich cathode materials [14], for example, L-NMC811 is the one that is most frequently mentioned for high-performance LIBs [12] [15] [16].

There are different synthesis methods to obtain Ni-rich cathode materials. Solid state method [17], sol-gel method [18], and co-precipitation then with solid state method [19], among them, co-precipitation with solid-state method are widely used in industry. In specific Li-NMC-O2 (lithium transition metal oxide powder) cathodes are usually synthesized by blending a lithium source with a Ni-Co-Mn precursor and heating in an oxygen atmosphere to produce lithium transition metal oxide powder, which has a stoichiometry of $LiMO_2$ (where M is the transition metal consisting of Ni, Co, Mn) [20]. Mixed transition metal precursors are used at the atomic scale for

NMC cathode preparation, typically in the form of MCO_3 carbonate form, or its oxidized form MOOH or hydroxide form $M(OH)_2$ hydroxide form [20]. NMC cathode crystal has a layered structure with Li and M layers in the R-3m space group [20]. NMC is a mixed metal cathode material that requires well-mixed Ni, Mn, and Co cations within the Li-M-O_2 crystal structure [20] to function properly.

These materials do, however, have certain technical difficulties as over time, L-NMC811 batteries' capacity may decrease, especially when operated at high voltages. As a result, battery life may be shortened, and replacement expenses may rise. Elevating the proportion of nickel content has the potential to enhance the initial discharge capacity [21]; However, it also results in significant decrease in the capacity as the electrode is subject to successive cycles of charge and discharge [21]. Ni-rich NMC compounds exhibit a proclivity towards undergoing thermal phase transitions to spinel and rock-salt structures, accompanied by the liberation of oxygen [21]. The process of oxygen discharge in batteries may result in the overheating of the battery, particularly in the event of excessive charging [21]. The purity of the L-NMC811 cathode precursor material is the key factor in the performance and security of the cathode materials after lithiation [22]. Impurities (such as S, Na) in the precursor material can cause problems with the cathode's structure, reduced capacity, and safety issues [22].

To solve these problems, doping is a strategy widely utilized in both academic and industry. Where doping in short, is a method of modifying electrode material properties. Cationic doping is one of the doping types [23]. This means we replace some of the metal ions in the material with different elements. Currently, a significant volume of research explores the incorporation of minor dopants into the Li-NMC811 structure, investigating their positive impact on crystal structure, electrochemical performance, thermal stability, and safety attributes. These positive effects enhance the suitability of the L-NMC811 structure as an appealing option for employment in high-performance LIBs. The administration of performance-enhancing substances has been shown to augment the electrochemical characteristics of the Li-NMC811 cathode, increasing its capacity, cycling stability, and rate capability [3].

Therefore, research on the cathode precursor material P-NMC811 is crucial to develop new and better cathode materials for a variety of applications as well as to improve the performance, cost-effectiveness, and safety of the L-NMC811 cathode materials [22]. This literature review section provides a comprehensive analysis of battery chemistry fundamentals, with a particular focus on several types of LIBs additionally, the current state of the battery market, and an analysis of the current structure and bonding of P-NMC811 by using XRD and Raman spectroscopy.

2.1 Fundamentals of battery chemistry

The LIB, which has the potential to revolutionize the world of energy in the twenty-first century, was commercialized in 1970s, even though we live in a time of constant invention and technological advancement. A battery is a mechanical system that converts chemical energy into electrical energy by storing it [24]. In general, active components mainly include the electrolyte, cathode, and anode. When the battery is connected to an external circuit, chemical processes take place in all of these variously constructed components. Also, as shown in Fig. 1, LIBs come in different configurations based on their geometric shape, like, a) cylindrical cells, b) coin cells, c) prismatic cells, and d) thin and flat cells [25].

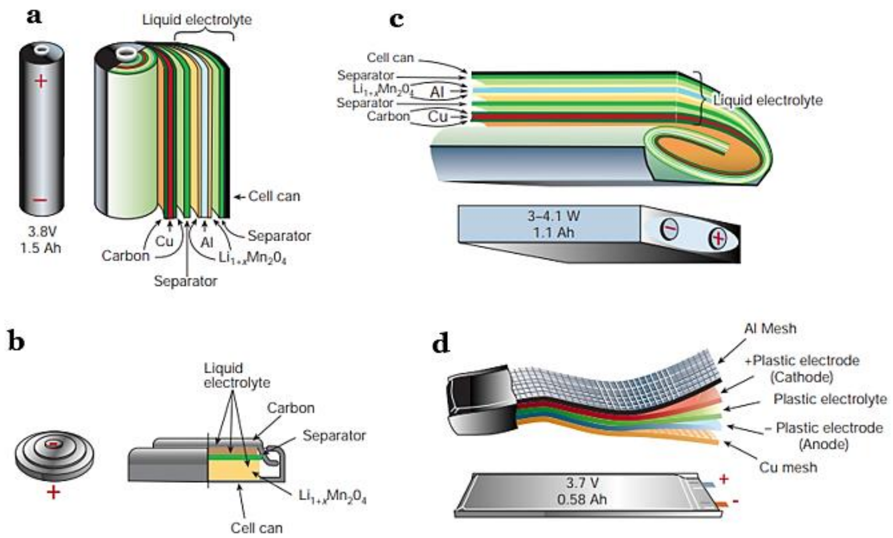

Figure 1: LIBs different configurations [25]

When classifying batteries for various applications, and in comparison, to lead-acid batteries, LIBs typically necessitate less maintenance. While it is accurate that LIBs often exhibit a longevity of over 4,000 charge-discharge cycles [24], it is essential to acknowledge that the specific cycle life can vary contingent on the battery's chemical composition and operational conditions. Furthermore, LIBs are renowned for their higher energy efficiency during the recharging process, resulting in lower energy requirements for efficient recharging. Additionally, they possess a superior energy density, enabling them to store a greater amount of energy and operate for extended durations between recharge cycles [24].

LIBs continue to outperform other battery technologies due to their excellent energy density and high charge/discharge efficiency, maintaining peak performance over extended periods [26]. However, their lifespan depends on various factors, including usage conditions and application complexity. To address this, electric vehicles (EVs) batteries can find a second life after their initial purpose is served. As many EV batteries are retired, repurposing them can enhance the cost-effectiveness of energy storage. Even if these reused modules may not perform optimally under all conditions, they can still serve auxiliary purposes. Additionally, repurposing these batteries can contribute to efficient energy storage in locations where traditional utilities and power systems face challenges [26].

2.2 LIB positive electrode chemistries

A common configuration for LIBs is the inclusion of multiple electrochemical cells that are electrically interconnected. When the battery is plugged in with an electric supply, the Li^+ ions tend to move from the cathode to the anode through the electrolyte as shown in Fig. 2. This is known as charging the battery. During the discharge phase of the battery, the movement of the Li^+ ions get reversed from anode to cathode through the electrolyte medium, and the electrical energy gets transmitted to the attached load. LIBs enable the conversion of chemical energy to electrical energy during discharging whereas, during charging, it transpires in the reverse direction via redox reactions [27].

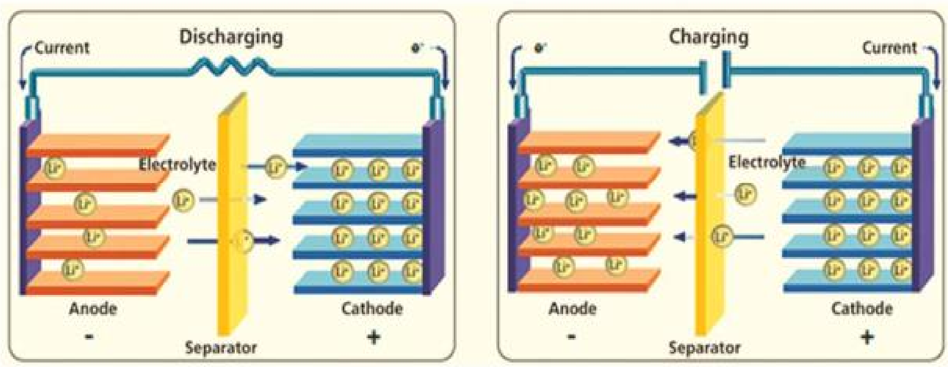

Figure 2: LIBs charging-discharging current flow [27]

The topic of which LIB type is superior and by what standards is then raised. Not all LIBs are made equal because there are numerous chemical combinations of lithium with other materials that have varied attributes such as specific energy, safety, performance, cost, specific power, and lifetime. Among the many different kinds of LIBs are those made of lithium nickel cobalt aluminium oxide ($LiNi_{1-x-y}Co_xAl_yO_2$, NCA), lithium cobalt oxide ($LiCoO_2$, LCO), lithium magnesium oxide ($LiMn_2O_4$, LMO), lithium iron phosphate ($LiFePO_4$, LFP), lithium nickel manganese cobalt oxide ($LiNi_{1-x-y}Mn_xCo_yO_2$, NMC), and others as shown in Fig. 3. It is possible to analyze the strength and improvement area for each cathode materials. For instance, in applications demanding high energy density and power density, cathode chemistries such as NMC and NCA are considered optimal. However, if added safety and cost-effectiveness are prioritized, NMC holds a slight advantage over NCA. When selecting batteries for diverse applications, a thorough analysis based on these parameters is instrumental in determining the most suitable choice for the intended application.

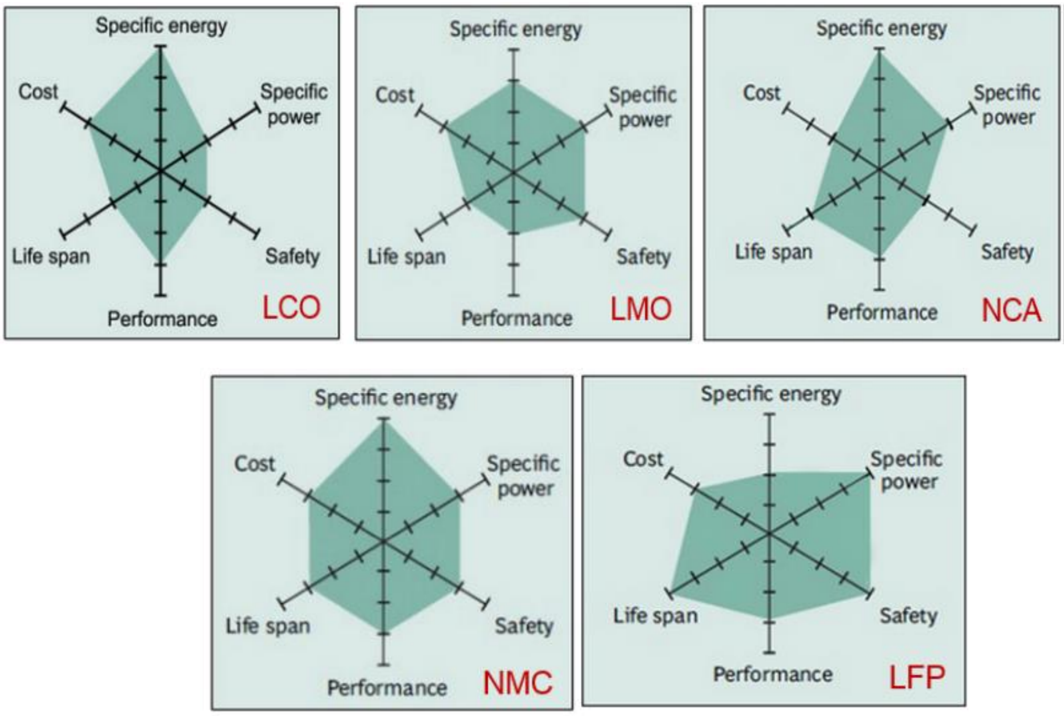

Figure 3: LIBs positive electrode chemistries and their features [28]

2.2.1 LCO battery

The composition of the battery is comprised of a cathode consisting of LCO and an anode made of graphite carbon. During discharge, the flow of lithium ions from the anode toward the cathode can be attributed to the layered structure of the cathode. Upon the initiation of charging, the direction and rate of the flow undergo alterations. The LCO batteries exhibit a specific energy around 150-200 Wh/kg [29]. Fig. 4 shown below is the layered crystal structure of LCO. With this configuration during cycling, Li^+ ions are removed and added to create vacancies in lithium planes. These batteries are known for their ability to provide sustained electric power over extended periods. However, they can face challenges when subjected to high-load conditions. Notably, LCO batteries offer a distinct advantage with their significantly higher specific energy when compared with lead acid batteries for example, allowing for continuous energy supply even during periods of reduced demand. Nevertheless, the declining popularity of LCO batteries can be attributed to several notable limitations, for example the energy density is not enough to be used for EVs. It has been noted that LCO batteries have a relatively short lifespan, usually lasting 500 to 1,000 cycles, however, considering the amount of cobalt required is not feasible for EV applications [30].

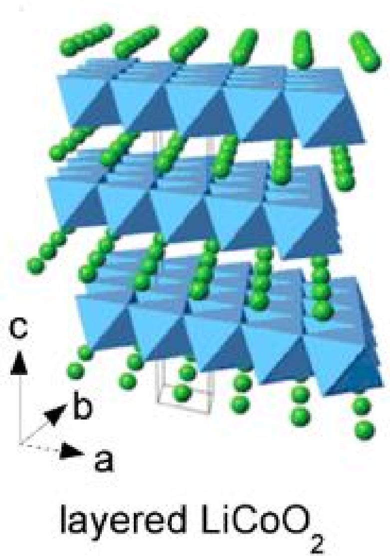

Figure 4: Crystal structure of LCO [31]

On the other hand, the element cobalt is recognized to exhibit a considerable level of economic significance within the contemporary market. Procuring expensive batteries with restricted longevity is not a fiscally feasible alternative [29]. Although initially popular, the demand for Li^+ ion batteries containing cobalt has declined due to the high cost of cobalt and safety concerns. Consumers are increasingly showing interest in alternative variants of LIBs, consequently leading to their growing popularity. The employment of LCO batteries is a widespread practice in portable electronic equipment, including but not limited to, cameras, tablets, laptops, and smartphones [30].

2.2.2 LFP battery

In LFP batteries, lithium iron phosphate serves as the cathode material, while a carbon-based electrode, often graphitic carbon, functions as the anode. The LFP batteries exhibit desirable thermal stability and electrochemical performance, rendering them suitable for extended usage owing to their prolonged life cycle. The structure has a distorted hcp oxygen framework with Li, Fe, and P ions occupying various sites as shown in Fig. 5. The FeO_6 octahedra are distorted, resulting in a lower symmetry. This figure shows channels for removing lithium ions. FeO_6 octahedra are linked in the bc-plane, while LiO_6 octahedra form chains along the b-axis. The PO_4 groups connect layers of FeO_6 octahedra through shared edges with one FeO_6 and two LiO_6 octahedra [31]. The energy density of LFP is around 90-160 Wh/kg [29]. LFP battery cells are equipped with a nominal voltage of 3.2 V [30]. As a consequence of this, LFP batteries represent the predominant type of lithium battery utilized as a substitute for lead-acid deep-cycle batteries. Despite being charged to full capacity, LFP batteries have been found to possess exceptional safety characteristics as compared to other lithium-based batteries owing to their high thermal runaway threshold, which is estimated to be around 518 °C [30]. However, the utilization of LFP batteries is associated with certain imperfections.

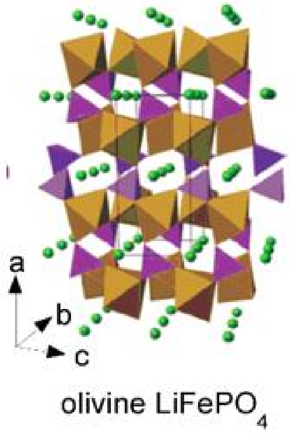

Figure 5: Crystal structure of LFP [31]

The degradation of the LFP cathode encompasses an extensive scope of both chemical and physical processes. The most significant mechanisms of degradation comprise the decay of active LFP and the deterioration of the cathode-electrolyte interface (CEI) [32]. The primary drivers of the aforementioned factors are the depletion of lithium supply, dissolution of iron, cathode detachment, or loss of contact with LFP, all of which stem from Al current collector corrosion, LFP particle cracking, and thermal gradients [32]. LFP batteries may not inherently excel in specific high-cranking applications due to their low specific energy along with decreased performance in cold environments [32].

2.2.3 LMO battery

The LMO is classified as a member of the $A[B_2]O_4$ spinel-type crystal structure, which is characterized by its arrangement of atoms. Specifically, LMO adopts the Fd-3m space group and exhibits a cubic lattice parameter with a value of a = 8.239 Å. The structure of cubic spinel LMO has been delineated, with Mn cations occupying the 16d sites and Li cations occupying the 8a sites, as shown in Fig. 6. Additionally, the oxygen ions are arranged in a nearly perfect cubic close-packed (ccp) sublattice, typically located on the

32e sites. A three-dimensional (3D) framework comprising MnO_6 octahedra that shares edges is formed as half of the octahedral interstices are occupied by Mn ions. The tetrahedral sites are occupied by Li^+ ions, and these sites are close to four neighbouring empty octahedral sites located at the 16c position with which they share common faces. This particular lattice provides a complex 3D structure consisting of 16c-8a-16c transport paths that enable the diffusion of lithium ions during insertion and deinsertion reactions [31].

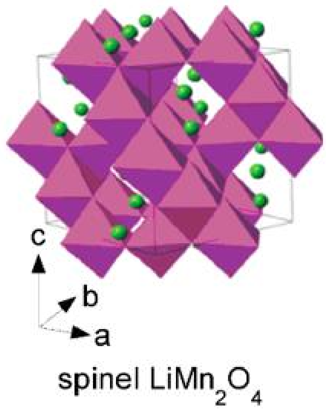

Figure 6: Crystal structure of LMO [31]

LMO batteries exhibit superior specific power and prompt charging capability [31]. Hence, they possess the ability to furnish higher current output in comparison to batteries employing LCO as the cathode materials. An added benefit of LMO batteries is their capacity for adaptability. The internal chemistry of LMO batteries can be adjusted to cater to applications demanding high-load or extended lifespan [30]. The most significant limitation of LMO batteries is their limited lifespan. LMO batteries are known to possess a relatively shorter lifespan when compared to alternative lithium-based battery types, with approximately 300-700 charge cycles being the average [30]. LMO batteries are commonly utilized in various modern applications including portable power tools, medical equipment, as well as certain hybrid and electric vehicles [30].

2.2.4 NCA battery

$LiNi_xCo_yAl_zO_2$, NCAs, with compositions where $x \geq 0.8$, and $x + y + z = 1$, are commonly referred to as 'nickel-rich' cathode materials for LIBs. These materials have gained significant attention and value in the battery industry for several compelling reasons, primarily centered around the reduced cobalt content they offer. This reduction in cobalt content makes these materials more economically attractive for large-scale battery manufacturing. Thus, the move towards cathode materials with lower cobalt content not only benefits cost-efficiency but also promotes sustainability and ethical standards in the battery industry. The present study elucidates the structural similarity between NCA and NMC, which exhibit layered α-$NaFeO_2$ structures. Notably, despite a minimal variation in the ionic radii of Al^{3+} and Mn^{3+} (0.0535 nm and 0.053 nm, respectively), the resulting NCA and NCM compounds showcase remarkable homogeneity in terms of their structural attributes. Based on pertinent scholarly studies, if the nickel concentration remains constant, the structural stability of NMC outperforms that of NCA. However, if the compositional ratio is $LiNi_{0.8}Co_{0.15}Al_{0.05}O_2$, NCA demonstrates superior electrochemical performance [33] and the cell structure of NCA with Co=0.15 is as shown in Fig. 7.

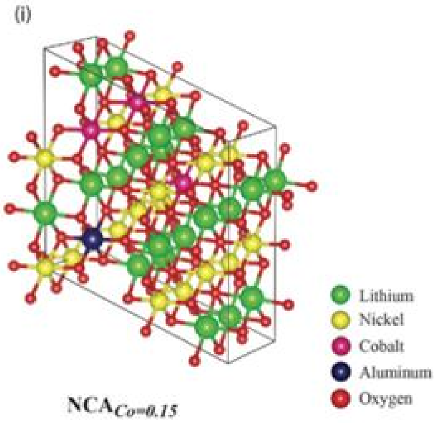

Figure 7: Optimized unit cell structures of NCA with Co=0.15 [34]

Besides, as the nickel substance share increases, so does the voltage and in this way the vitality that can be put away within the battery. The most notable advantages offered by NCA batteries are their high energy density and above-average lifespan. NCA batteries degrade and lose capacity/power when cycled [35]. When a normal NCA battery is warmed to 180 °C, it'll thermally run away [30]. NCA batteries are highly regarded in the electric vehicle (EV) market due to their ability to endure high-stress applications and maintain a significant amount of charge for extended periods. Tesla incorporates NCA batteries alongside other battery types in their EVs [30].

2.2.5 NMC battery

NMC batteries possess the advantage of amalgamating the favourable aspects of the principal components incorporated in the cathode, namely nickel, cobalt, and manganese. NMC materials have a structure with layered transition metal cations and lithium ions between them [36] as shown in Fig. 8. The types of NMC cathode materials are referred to as NMC111, NMC532, NMC622, and NMC811. The numeric designation that succeeds the acronym NMC denotes the relative mole concentration of nickel, manganese, and cobalt present within the cathode. The evolution of a cathode is contingent upon the quantity of nickel present within its layer. Numerous original equipment manufacturers (OEMs) have initiated the commercialization of NMC cathodes that contain less cobalt [37].

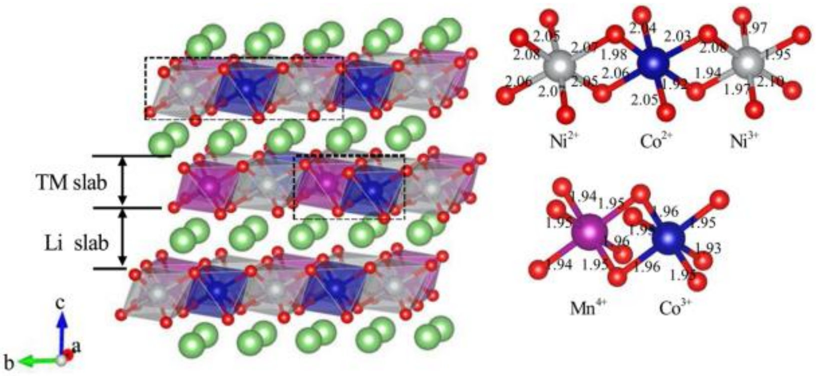

Figure 8: Crystal structure of NMC [38]

In comparison to LCO batteries, they exhibit superior thermal stability, ultimately rendering them a safer alternative. NMC batteries are widely utilized in the domains of power tools, electronic powertrains for e-bikes, scooters, and a subset of electric automobiles. One significant distinction is that NMC batteries tend to exhibit superior thermal stability compared to LCOs, making them a safer choice for certain applications [31].

2.3 Synthesis methods of NMC cathode

The synthesis part is covered in this report to emphasize how these approaches are significant as they enable the manufacturing of high-quality NMC cathode materials with regulated morphology, particle size, and composition, all of which are critical aspects of LIBs' performance. There are different methods to synthesize NMC cathode materials, sol-gel method [39], co-precipitation method with solid-state method [39], solid-state reaction [39], spray pyrolysis and also hydrothermal synthesis [39], as shown in Fig. 9.

Among the various methodologies available, co-precipitation method for precursors is widely regarded as the preferred method due to its low cost, ease of managing process parameters, and ability to achieve high tap densities, and already widely used in industry [40]. The precipitation reaction progress, the mixing speed, chelating agent concentration, pH level, the around temperature are all variables that can greatly impact the shape and composition of the particles during the co-precipitation process [40], and after which NMC precursor materials are obtained. Then, precursor will be mixed with LiOH or Li_2CO_3 and calcine in high temperature to obtain NMC cathode materials.

Solid state method is considered to be one of the earliest and simple techniques recorded in the literature for the synthesis of active materials for batteries [40]. This approach has garnered significant attention in the industry for producing nanoscale NMC cathode materials owing to economical equipment requirements and straightforward process management. The process of synthesis is characterized by its simplicity, whereby the fusion of transition metal oxides and Li salt occurs through sintering at temperatures within the range of 800-1000 °C [40]. This method presents a prominent benefit as it facilitates the attainment of precise stoichiometry about lithium and transition metals. However, it entails rigorous mechanical blending and prolonged thermal processing [40].

The spray pyrolysis technique represents a versatile approach for the production of cathode materials based on NMC compositions on a large scale, exhibiting a notably high level of reproducibility [40]. The technological process known as spray pyrolysis is a continuous synthetic technique that offers various advantages, such as a brief residence time, a high degree of purity, and a limited range of particle sizes. Despite these benefits, it is prone to the creation of hollow and shell-like particles, which can significantly diminish the tap density. In general, co-precipitation is found to be the optimal technique for batch manufacturing of NMC precursor material, whereas spray pyrolysis is deemed as the most suitable method for continuous production [40].

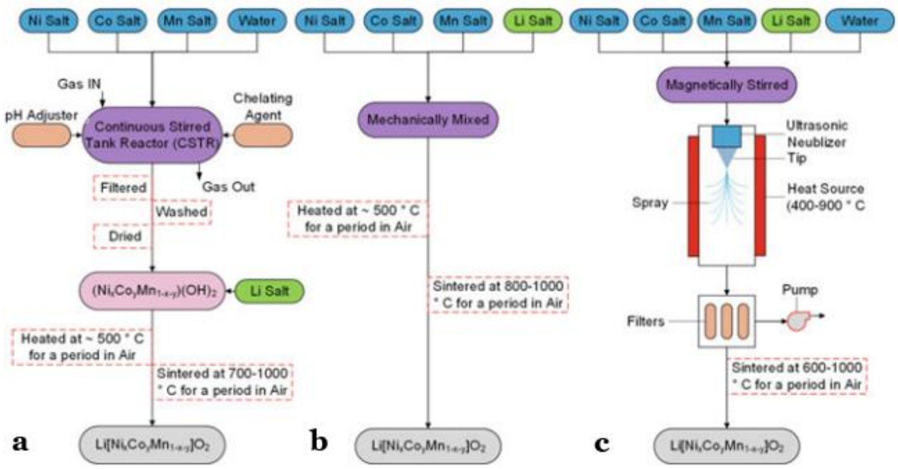

Figure 9: Few of the NMC cathode synthesis methods a. co-precipitation, b. solid state, c. spray pyrolysis [40]

2.4 A comprehensive overview of the battery industry

Numerous studies that concentrate on understanding battery future trends and how they will affect society while taking supply and demand and the supply chain into account have been conducted for more than ten years. Since my thesis work is related to NMC battery technology, the market study is related to its advancement in raw materials available, and consumption rate in the future. According to the projections of Bloomberg new energy finance, a significant increase in the sales of electric vehicles is anticipated, with figures predicted to exceed 60 million by the year 2040 and a staggering 190 million by 2050 [41]. The widespread utilization of LIB in portable devices intended for consumer use has resulted in a remarkable increase in the production of these batteries, as evidenced by the fact that in the year 2020, the amount of these batteries manufactured exceeded 25 billion units, occupying a weight equivalent to 500 thousand metric tonnes. Anticipated are increased trajectories regarding the installation and sales of consumer electronics and stationary energy storage (SES). Upon examination of the extraction and processing procedures, it becomes evident that a majority of the crucial elements are exclusively manufactured in a limited number of select nations as shown in Fig. 10. In the year 2021, the total global cobalt production amounted to 170,000 metric tonnes. Of this total volume, the majority - approximately 71% - was obtained from mining operations in the democratic republic of Congo [42]. Meanwhile, mining activities in Russia contributed 4.5% of the total cobalt production, and the remaining 3.3% was produced within the geographical confines of Australia. The majority of cobalt is extracted as a secondary product during the mining process of copper or nickel. It is a well-established fact that the majority of significant cobalt-bearing deposits are situated within the central African copper belt region. Over the years, numerous investigations have highlighted concerns surrounding the risks inherent in the artisanal mining sector, particularly concerning cobalt production in Congo, including the use of child labour. As a result, scholars have called for the implementation of secure, transparent, and verifiable supply chains and systems to effectively identify and address such potential dangers within the socially conscious mining industry [43].

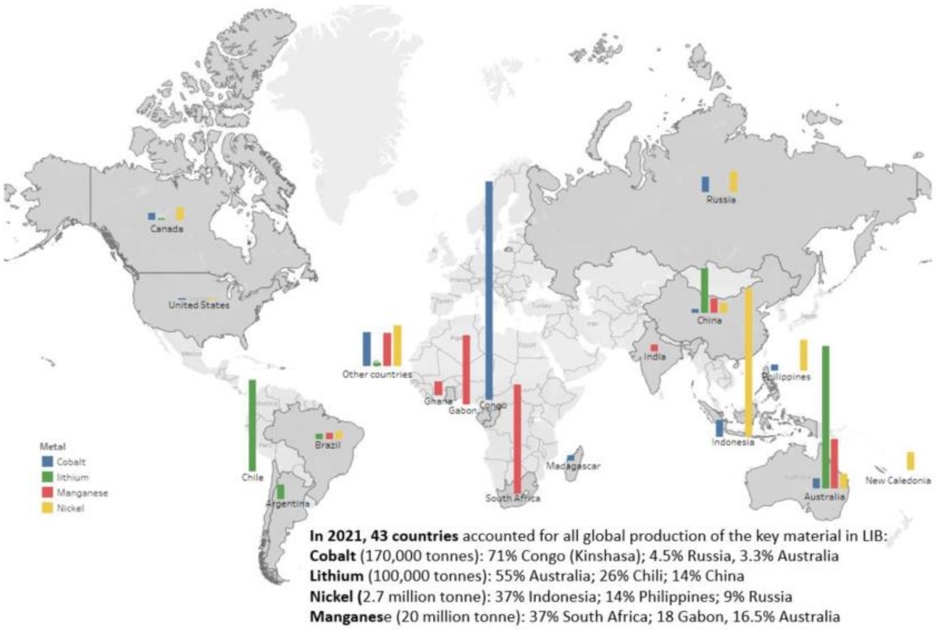

Figure 10: The lithium battery elements' key location of mining and extraction [43]

[44] The technical report on the battery market and forecast outlines the top battery cathode chemistries, evaluate their characteristics, and examines the market trends as shown in Fig. 11. The x-axis shows the amount of energy required to be spend for the given applications and y-axis indicate the overall performance rating. The automobile industry, which is predicted to have 89% of the market share by 2030, will continue to receive a lot of attention from the battery industry, while grid applications will experience rapid growth and more than quadruple their present market size to $10,8 Bn. The improvement of batteries might also lead to the opening of new markets for batteries, such as for electric airplanes, which might eventually experience the quickest growth. NMC and LFP are the best options for meeting the requirements of most electric vehicles, which include high energy density, satisfactory cycle life, and affordable battery costs.

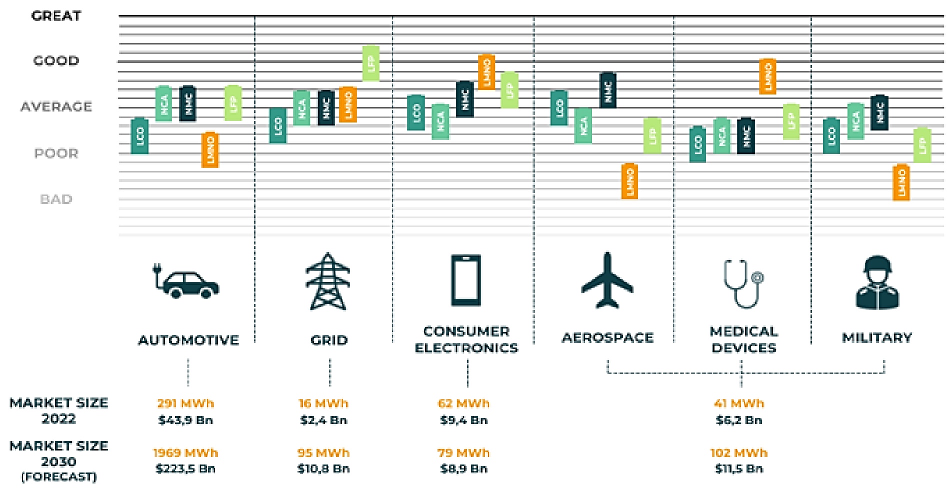

Figure 11: Market size 2022 and forecast 2030 [44]

Based on the findings of the market analysis, it is apparent that the battery sector exhibits significant growth opportunities. However, the application of batteries is currently constrained by the availability of raw materials, as well as the parameters surrounding their extraction and their ramifications on the circular economy. At present, batteries maintain a highly competitive cost. Nonetheless, they continue to exhibit limitations in several aspects, including energy density, cycle life, and safety considerations. One significant challenge confronting the battery industry pertains to the absence of an extensive system for recycling. The expanding usage of batteries has generated an increasing demand to devise resourceful and economical techniques to recycle them. The supply chain for essential materials, particularly lithium, cobalt, nickel, and manganese, poses a significant challenge [45]. The acquisition of these resources is frequently restricted to a finite group of nations, resulting in potential instabilities in supply chains and geopolitical hazards. NMC811 batteries possess distinct advantages that render them potential candidates for deployment in various applications in the future. However, despite their relatively greater stability, these batteries still face several challenges, including, but not limited to, the procurement of critical raw materials. Consequently, a critical aspect in comprehending the nature of NMC entails delving into battery cathode chemistry starting from the study of precursor structural properties and gaining insights regarding its chemical bonding and the inadequacies that exist within its present chemistry [45].

2.5 X-ray power diffraction

XRD will be one of the main technologies utilized in this study. A brief history and theory behind the XRD origins and early applications is provided here. The well-known experiment by Max von Laue, Friedrich, and Knipping in

1912 showed the diffraction of X-rays by crystals [46]. This discovery served as the starting point for later developments in XRD analysis. Renowned researchers like William and Lawrence Bragg created the equation known as Bragg's law that connects the angles of incidence and diffraction to the distance between crystal lattice planes. The Braggs were awarded the 1915 Nobel prize in physics for their scientific discovery, which made it possible to determine crystal formations. When XRD was originally used in the study of minerals, it helped scientists identify and categorize various minerals according to their crystal shapes. It also looks into the field of materials science, where understanding the arrangement of atoms and molecules in a variety of materials, such as polymers, metals, and ceramics, has been made possible through XRD research [47]. Later, advances were made using XRD techniques and technologies, such as the development of synchrotron radiation sources that produce powerful X-ray beams for more precise and complete analyses.

The concept of X-ray as shown in Fig. 12 goes like this, to bend electromagnetic radiation, the spaces in the grating must be similar in size to the wavelength. In crystals, the space between atoms is usually 2 to 3Å [48]. This means that a certain type of radiation is best suited for studying crystals. X-rays are a type of energy that can pass through objects. They are used in medical imaging to see inside the body. So, X-rays can help us learn about how crystals are built. Scientists study materials using neutrons and electrons for diffraction.

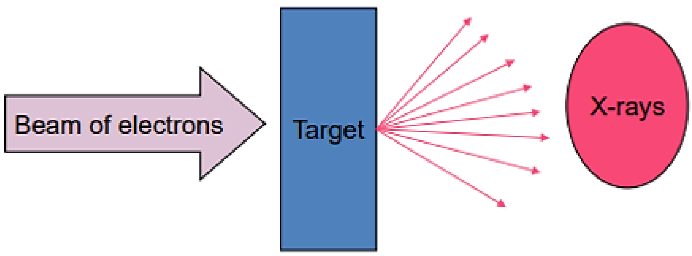

Figure 12: Concept of X-ray generation [48]

XRD has become a prevailing method for investigating crystalline materials [48]. The XRD method provides a valuable complement to a variety of microscopic and spectroscopic techniques. To evaluate potential microscopic observations made on a small scale, it is necessary to analyze the corresponding microscopy data. This analytical approach can be considered as an essential component of scientific investigation in various fields of study. This method will be used for the study aiming to contribute to the broader field of inquiry by shedding new light on the specific area under investigation, and by providing a basis for further research and exploration [49].

An image of the PANalytical scanning diffractometer is shown in Fig. 13a. The detector revolves around the sample. The position of the detector is recorded using the angle 2 theta (2θ). The device counts the number of X-rays that are detected at various 2 angles as shown in Fig. 13b. The quantity of X-ray intensity is often expressed in terms of "counts" or "counts per second." To keep the X-ray beam in the right focus, the sample will also spin. The Bragg-Brentano technique of para-focusing geometry is used by several powder diffractometers. Both the incidence angle omega (°) and (2θ) must be adjusted for the X-ray beam to be oriented correctly. A general overview of how exactly XRD data can be evaluated is explained here using a reference from a presentation made available by the Massachusetts institute of technology [50].

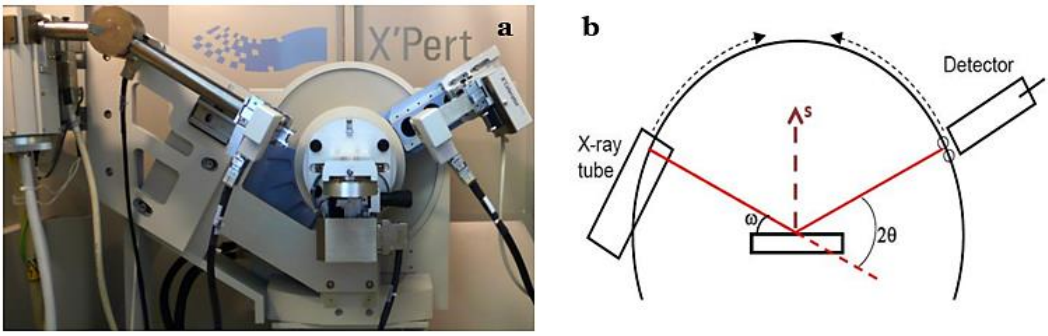

Figure 13: a. PANalytical scanning diffractometer X'pert Pro MPD alpha [51]; b. Bragg-Brentano para focusing geometry [49]

Fig. 14 a displays the XRD patterns of quartz, cristobalite, and glass, which are made up of several SiO_2 phases [50]. Despite having nearly identical chemical properties, they differ in their atom arrangements, which can be explained by the diffraction pattern. High crystallinity is demonstrated by the sharpness of the quartz pattern, and the amorphous nature of glass-like substances that do not create sharp diffraction patterns is revealed. It is also feasible to tell how many crystalline phases are present in the combination and whether any amorphous material or compound is present by looking at Fig. 14b, which shows the copper's XRD pattern.

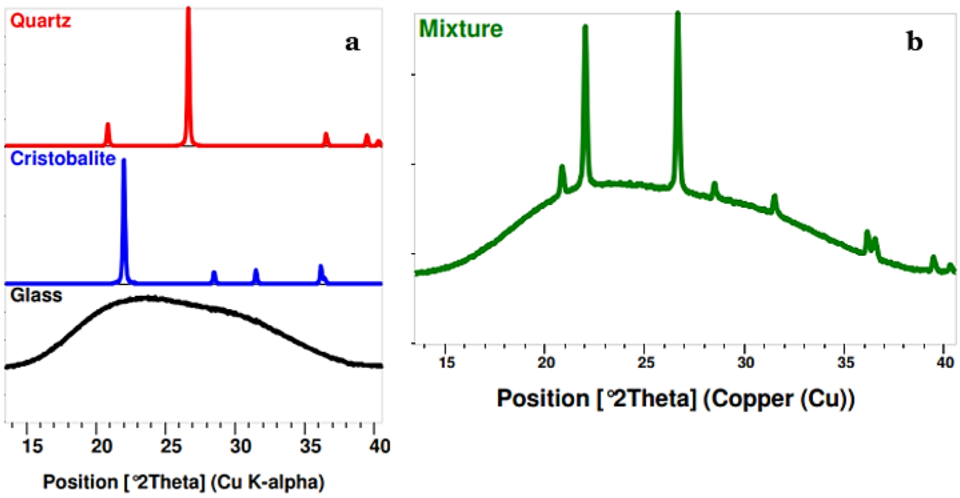

Figure 14: a. Different diffraction patterns of materials; b. Sample XRD plot of copper (Cu) [50]

The actual phases are typically determined by comparing the experimental pattern to a reference pattern. The peak positions of the reference pattern should also match the data; however, a slight experiment-related error is acceptable. The experimental data should also include all of the peaks from the reference pattern. The locations of the diffraction peaks can be used to calculate the dimensions of unit cells. It is feasible to convert the measured peak locations, 2θ, into d_{hkl} values using the previously mentioned Bragg's law. With this information and understanding other literature was looked into to understand how this technique was used to study and analyze the battery cathode materials, especially the L-NMC cathode chemistries.

As an example, Fig. 15 shows the XRD patterns of synthesized L-NMC811, and commercial L-NMC811 cathodes. It shows the lattice plane (003) has the highest peaks, the high-intensity peaks suggest crystalline phases with well-defined structures and precise atom arrangement. The intense signal indicates strong diffraction in highly crystalline material with many scattering centres. The XRD patterns' peak splitting validates the structure's layers [52].

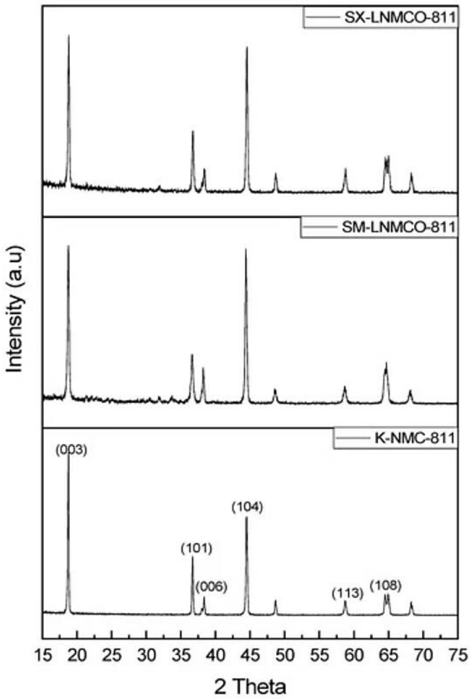

Figure 15: The XRD pattern of a Li-NMC811 cathode materials [52]

A study that aimed to study the co-precipitation of the $NMC811(OH)_2$ as a precursor was recently published [53]. XRD was used for analysing the crystal structure, crystallographic phases, lattice parameters, and crystallinity of the co-precipitated precursor material. In the literature, the data were analyzed using XRD, and some insightful conclusions were reached as a result. The author identifies the formation of secondary particles in the supersaturated solution during the synthesis of the P-NMC811. The XRD data was used to compare the diffractograms of the synthesized crystals and compared to the different total flow rates during the metal feed concentration of 1 M and $[M^{2+}]:[NH3]$ = 1:1. The XRD features include, a PANalytical X'Pert Pro (Cu K_α radiation, k = 0.154187 nm) diffractometer equipped with a 2D solid PIXcel detector. The author compiled the following findings using the XRD data from Fig. 16 a,b. The diffractograms of the three largest total flow rates were compared, and it is evident that as the flow rate rises, the XRD peak sharpness decreases, some peaks widen, and the crystallinity of the sample decreases. Additionally, the pure $Mn(OH)_2$ peaks at 28.6° and 54.04° of the precursor XRD peaks were missing, and the diffractogram resembles that of $Ni(OH)_2$. The author infers from references that Mn^{2+} substitutes for Ni^{2+} atoms arbitrarily in the $Ni(OH)_2$ lattice. And noticeable the XRD peaks of $Co(OH)_2$ was comparable with $Ni(OH)_2$ which made it difficult to justify the presence or absence of the Co^{2+} like Mn^{2+} [53]. Another inference that might be made from the analysis of the XRD is that the varied synthesis circumstances resulted in distinct crystalline structures for beta-$Ni(OH)_2$ and alpha-$Ni(OH)_2$ 0.75 H_2O. The crystalline size of $Ni(OH)_2$, peak broadening, stacking defects, and deviations in peak positions were all evaluated by the author using OriginPro software and the X'Pert HighScore Scherrer calculator's half-maximum intensity (FWHM). The research continued with the latest literature on evaluating the electrochemical performance with the structural design of the $NMC811(OH)_2$ precursor [54].

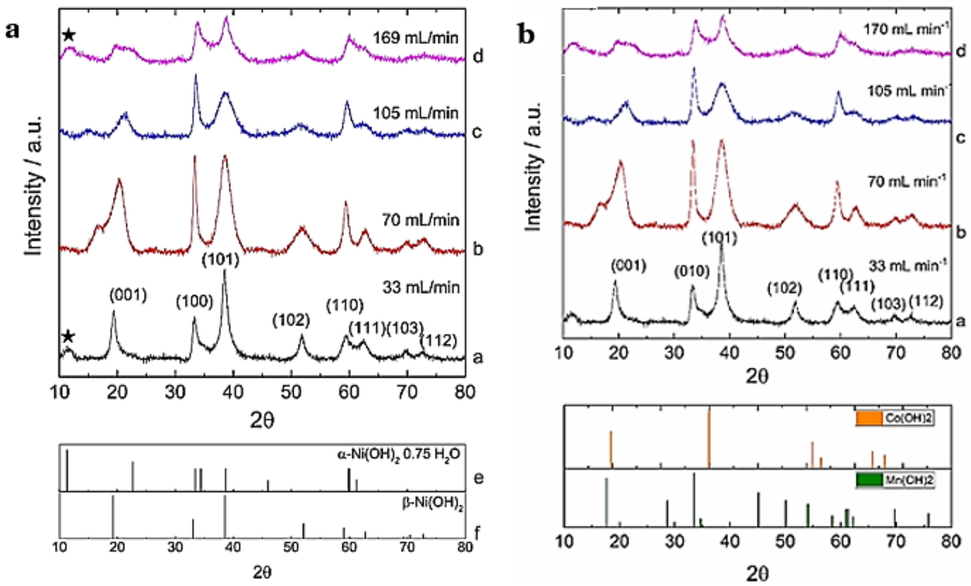

Figure 16: a. XRD patterns for synthesized crystals of $NMC811(OH)_2$ at various total flow rates of a) 33 mL/min, b) 70 mL/min, c) 105 mL/min, and d) 169 mL/min; b. XRD pattern of synthesized crystals compared to $Mn(OH)_2$ and $Co(OH)_2$ [53].

Another research paper was published by researchers on the synthesis of P-$NMC811(OH)_2$ and the electrochemical performance upon lithiated L-$NMC811O_2$ [55]. In this case, the XRD experiments were carried out on a diffractometer D/max 2550 X (Rigaku, Japan), using Cu Kα radiation (wavelength=0.154056 nm, voltage 40 kV, and current 300 mA), with a step size of 0.02° and a recorded range from 10° to 80°. The results obtained are as shown in Fig. 17, which show the highly crystalline peaks of the lithiated sample without any secondary peaks, and all peaks are indexed as hexagonal a-$NaFeO_2$ structure with a space group of R-3m.

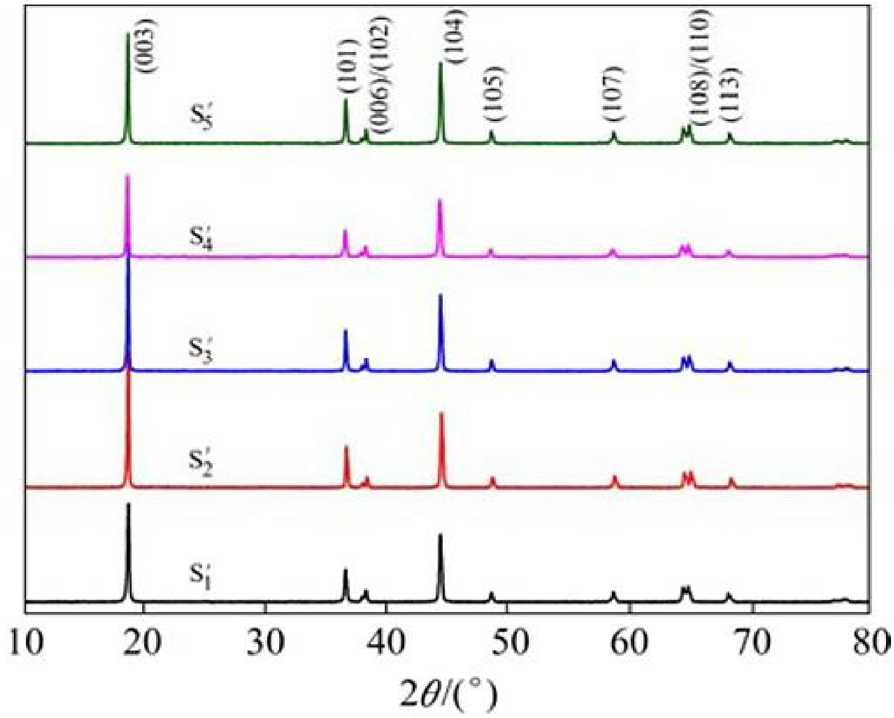

Figure 17: Li-NMC811 XRD pattern of samples prepared at 750°c [55]

There has also been research on the co-precipitation approach for the synthesis of $Ni_xMn_{1-x}(OH)_2$ mixed hydroxides as shown in [56]. The sample was created using several co-precipitation procedures, and XRD was utilized to analyze the sample structural analysis. The presence of air during the co-precipitation process, results in the creation of complex structures of layered double hydroxide (LDH) which are layered materials that contain positively charged metal hydroxide layers interlaced with anions and Mn_3O_4 phases. Using XRD data, the sample's structure was able to detect the arrangements of the atoms in each sample leading the way for further analysis as in Fig. 18.

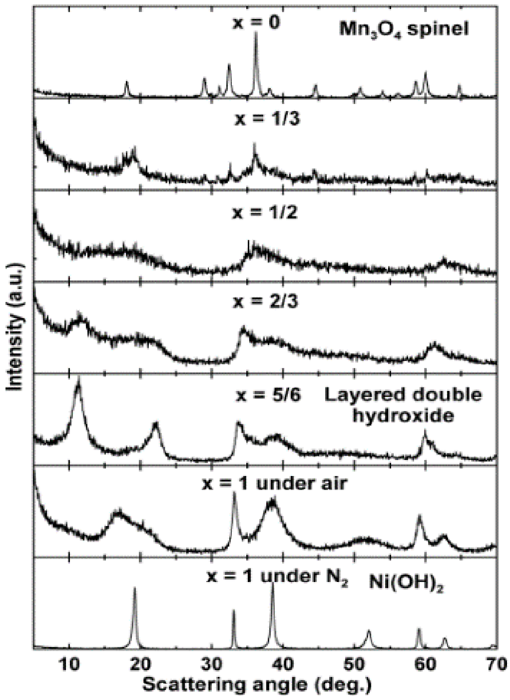

Figure 18: XRD pattern of $Ni_xMn_{1-x}(OH)_2$ samples [56]

A good takeaway from these reviews of the kinds of literature is that the XRD is a useful tool for examining the crystal structure and phase composition of a specific precursor throughout its synthesis conditions and providing essential information about the crystalline phases present. Also, upon the investigation of the lithiated sample, the secondary phases and defects can be investigated. Most of the research work was published based on the findings of the lithiated samples and very limited data is available related to the study of precursor and its properties and structure evaluated using XRD.

2.6 *In-situ* HT-XRD

In this section, the cathode precursor materials for LIB cells have been studied for structural alterations using *in-situ* HT-XRD, which is a significant tool and technology. It provides valuable information about the traits and behaviour of the material under various conditions. When employing *in-situ* HT-XRD to conduct experiments, the sample is subjected to conditions like alterations in the gas environment, pressure, and temperature, while the XRD data is continually gathered. These observations aid in the research and analysis of the modifications to crystal structure brought in by these conditions.

To illustrate its significance and characteristics, a study that used *in-situ* diffraction to look at the structural evolution of various lithium-deficient NMC cathode materials is provided as an example [57]. Fig. 19 shows the *in-*

situ HT-XRD plotted as a function of temperature for the P-NMC811 while heating in the presence of lithium.

The hydroxide precursors underwent the *in-situ* HT-XRD considering the following temperature profile. The test was conducted for the 2θ range of 15° to 68° and a temperature range of 0 to 900°C. Throughout the entire heat treatment, diffraction measurements were taken in the 2θ range of 15° to 68° at intervals of 5 minutes. The final temperature was attained by gradually heating the precursor powders in an air environment at a rate of 4°C per minute, following a previous heating process in the air at a rate of 5°C per minute until reaching 450°C. Each pattern was measured with a step size of 0.0394° 2θ and a count time of 47.7 s per step. In the case of NMC811, the reaction pattern seems to involve the progressive conversion of metal hydroxides to metal oxides and then to complex metal oxides [57]. The disintegration of the LiOH precursor starts at 210°C and ends with the synthesis of LiO_x at 418°C. When the temperature reaches 503°C, the complex metal oxides react with the liquid oxygen to form $LiMn_{1.34}Co_{0.66}O_4$ and $Li_{0.28}Ni_{0.72}O$ [57]. Also, it was noticed that there has not been much literature related to *in-situ* HT-XRD being used to analyze the NMC811 precursor and related.

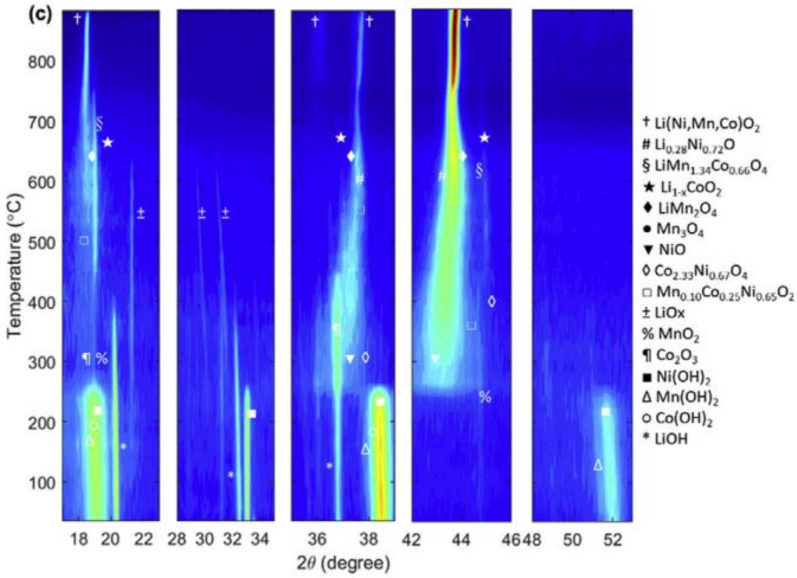

Figure 19: *In-situ* HT-XRD of NMC811 precursor heated in the presence of lithium source [57].

2.7 Raman spectroscopy

Raman spectroscopy assesses a material's energy modes using light, named after C. V. Raman and K.S Krishnan observed Raman scattering in 1928. S. Krishnan. Raman spectroscopy provides chemical and structural information and identifies compounds by their unique Raman "fingerprint" through the detection of Raman scattering.

In this concept, as shown in Fig. 20 a photon turns a molecule polar, transferring energy in the process, and forming a transient complex known as the virtual state. The photon is swiftly reemitted as dispersed light because the virtual state is unstable [58]. The energy of the molecule typically stays constant. Therefore, the input photon's energy and wavelength are carried over into the scattered photon. The energy of the scattering particles is preserved in Rayleigh scattering. Rarely, energy is transferred between molecules and photons during a process called Raman scattering. When a molecule gains energy, the scattered photon experiences Raman scattering, which results in a loss of energy and an increase in wavelength. Approximately 1 in 10 million photons experience Raman scattering [58]. If the molecule relaxes and loses energy, the scattered photon gains energy and its wavelength shortens, a phenomenon known as Anti-stokes Raman scattering when molecules are excited from their ground state to a virtual state and then relax into a vibrationally excited state, they exhibit the spontaneous Raman effect, which is represented by Stokes Raman scattering [58].

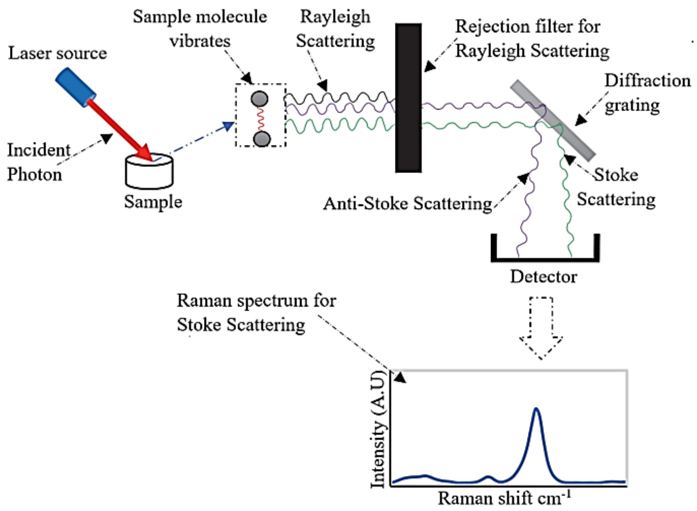

Figure 20: Systematic diagram of Raman spectrometer instrumentation [59]

The Raman spectrum is characterized by the presence of multiple peaks that provide information regarding the intensity and position of the wavelength of Raman scattered light. Each zenith is linked with a specific chemical bonding vibration, comprising solitary bonds such as C-H, N-O, C=C, and C-C along with bond groups such as the benzene ring's respiration mode, polymer chain oscillations, lattice modes, and others [60].

Currently, Raman spectroscopy finds widespread use in the field of chemistry, where it is applied for the investigation of structural features, purity assessment, and monitoring of chemical reactions. Additionally, its utility extends to the realm of pharmaceutics, where it is employed for the study of content uniformity, component distribution, and related applications. Furthermore, Raman spectroscopy is utilized for the analysis of carbon materials for purposes such as examining the structural and compositional purity of nanotubes, and detection and characterization of disorder, etc.

Fig. 21 shows the Raman spectroscopy developed by Renishaw; features include Raman microscopy that could distinguish chemical structures with high spatial resolution. Microscope techniques including brightfield, darkfield, and polarization contrast with reflected and transmitted light. Particle analysis uses image recognition algorithms and instrument control to characterize distributions and many more [61].

Figure 21: Raman spectroscopy by Renishaw [61]

A study was conducted to understand the Raman shift and analyze the spectrum of Li-NMC111 chemistry [62]. The Raman spectrum, which can also determine the existence of impurities or secondary phases, is used to determine the purity of the phases in Li-NMC111 samples. It is typical to discover impurities or secondary phases that exhibit various Raman peaks from Li-NMC111 [62]. Typically, it is found that the size of the particles in the sample has an inverse connection with the width of the Raman spectra. In this case, as shown in Fig. 22, two broad Raman bands of the carbon caused by MWCNTs are associated with the D-band, G-band, and 2D-band at 1380, 1589, and 2700 cm^{-1}, respectively. The Ni-O mode at 471 cm^{-1} and the broadband at 599 cm^{-1} are vibrational features of Li-NMC111 [62].

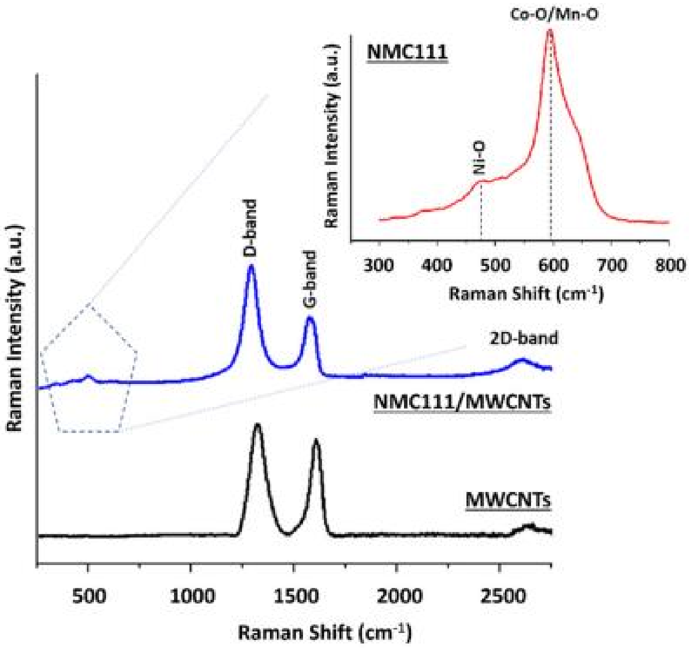

Figure 22: NMC111 powder Raman spectra [62]

Raman spectroscopy has also been used in the battery manufacturing industry to detect the presence of contamination during the battery production process [63]. In this case, Raman spectroscopy was used to compare batches of battery-grade lithium hydroxide salts to check for carbonate impurities. In Fig. 23, the red Raman spectrum shows that there is no presence of any impurities, whereas in the plots that belong to the spectra blue, green, and violet indicate the presence of carbonates at a shift range below 200 and above 1000 cm^{-1}. So, this brings us to a point to show how these spectra images can interpret the data to showcase the presence of secondary particles in a given sample. Besides, when using Renishaw Raman spectroscopy for testing, it's important to remember that sensitive samples can easily get damaged when the laser power is not controlled [64]. By increasing the energy of the laser beam that is used, the Raman signal that is produced can be made stronger. There is different strength of lasers in Raman system. By choosing the weaker lasers, it can prevent sample damage.

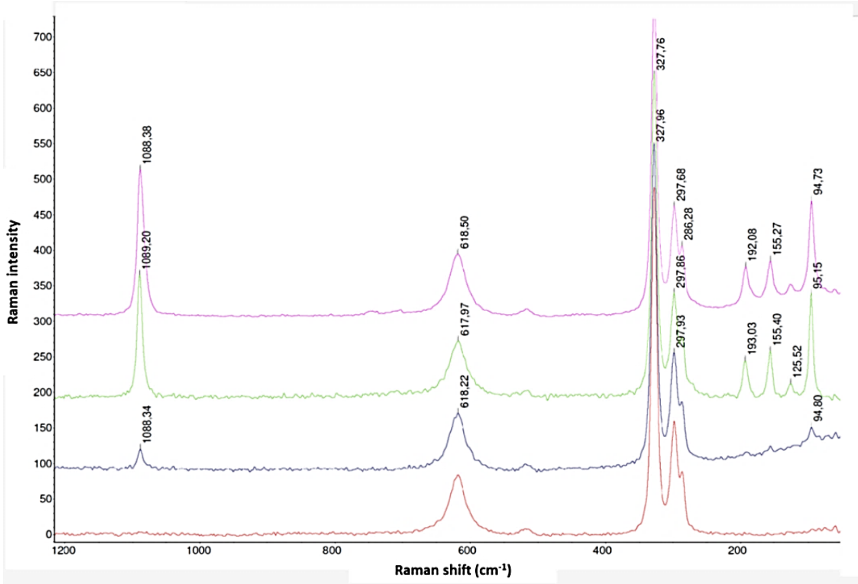

Figure 23: Raman spectroscopy that was used to compare different batches of battery-grade lithium hydroxide salts [63]

The utilization of XRD facilitates comprehension regarding the crystal structure, lattice parameters, and phase purity of P-NMC811. Similarly, Raman spectroscopy can offer insight into the vibrational modes and thermal stability of the aforementioned material. Collectively, these methodologies exhibit potential for enhancing the synthesis and processing of L-NMC811 cathode materials [62], as well as appraising their performance in LIBs. This inquiry pertains to the potential outcomes that could be achieved through the execution of these studies for a thesis, including the examination of the P-NMC811's features and composition, and the exploration of ways in which it can be enhanced through this investigative process [62].

In this section, the literature review of LIBs, cathode materials for LIBs, and the utilization of XRD and Raman spectroscopy in cathode materials are involved. However, it is worthy to mentation that there is no research related to Raman spectroscopy usage to analyse the P-NMC811. And there is very limited information about the P-NMC811 using XRD, therefore, it is necessary to investigate P-NMC811 properties by XRD and Raman spectroscopy.

3. Experiment methodology

The main objective of this thesis work is to investigate the precursor properties. In specific limitation to detect the P-NMC811 secondary phases by utilizing the laboratory's XRD and Raman spectroscopy equipment. Following that, a mixture comprising a range of quantities of MoO_3 (99.5%, Alfa Aesar), $Al(OH)_3$ (Merck), and $Zr(OH)_4$ (97%, Sigma-Aldrich) compounds will be combined with the precursor substance, and the existence of compounds and the secondary phase will then be examined. For $Mg(OH)_2$ (99%, Sigma-Aldrich) , only the XRD spectrum was captured and was not mixed with precursor for investigation. It is because the precursor XRD peaks match closely with peaks of $Mg(OH)_2$, so it was difficult to detect the secondary phases. The sample lists are in Table 1. Also, all these samples were prepared for the same 1-gram quantity of precursor.

Table 1: Sample list of sample preparation

Sl.no	Precursor + Compound	Precursor (g)	Compounds (g)	Representation for Analysis
1	$Ni_{0.8}Mn_{0.1}Co_{0.1}(OH)_2$ (P-NMC811)	1	-	NMC811 precursor/NMC811
2	$Mg(OH)_2$	-	1	$Mg(OH)_2$
3	P-NMC811 + $Zr(OH)_4$	0.98	0.02 (2%)	$2Zr(OH)_4$-NMC811
		0.95	0.05 (5%)	$5Zr(OH)_4$-NMC811
		0.5	0.5 (50%)	$50Zr(OH)_4$-NMC811
4	P-NMC811 + MoO_3	0.99	0.01 (1%)	$1MoO_3$-NMC811
		0.995	0.005 (0.5%)	$0.5MoO_3$-NMC811
		0.999	0.001 (0.1%)	$0.1MoO_3$-NMC811
5	P-NMC811 + $Al(OH)_3$	0.99	0.01 (1%)	$1Al(OH)_3$-NMC811
		0.995	0.005 (0.5%)	$0.5Al(OH)_3$-NMC811
		0.9975	0.0025 (0.25%)	$0.25Al(OH)_3$-NMC811

3.1 Sample preparation

The compounds are chosen to have their melting point near the lithiation temperature of 750 to 850°C [65], in this case, MoO_3 (Melting point of 795°C [66]), $Zr(OH)_4$ (melting point of 550°C [67] , $Al(OH)_3$ (melting point of 300°C) [68] , and $Mg(OH)_2$ (melting point of 350°C) are chosen for the investigation. The melting points are specified because they significantly affect how dopants can blend and infiltrate the precursor during lithiation stage. These factors are vital for consistently and effectively altering the material's properties.

The P-NMC811 material is then combined with a small quantity of the aforementioned compounds using mortar and pestle as shown in Fig. 24 Standard procedure used for mixing all the sample is 30 min. By hand-grind with a mortar and pestle, a sample of a mixture is first examined to determine whether any secondary phases are present. The target is to identify the secondary phase of the precursor, and the selection of additional compound quantity based on the XRD detection.

Figure 24: Mortar and pestle [69]

3.2 Structure of precursor studied using PANalytical X'pert Pro MPD Alpha 1

The initial step is to identify the amount of sample that could be tested in the X'pert XRD as shown in Fig. 25, by checking the sample holder weight with the sample minus the weight of the holder. In this case, it's measured to be 1 gram of the sample that is needed for testing and kept constant. Set X-ray wavelength (Cu Kα), scan range (2θ), and speed. For the testing, the following settings were used, start angle =10°, end angle = 90°, step size = 0.01313°(2θ), at 40 kV and 40 mA, time per step =130.05 s, scan speed = 0.0257 °/sec, total number of steps = 6092. Data is then analyzed with software Match 3 [70] to identify the crystal phases and the plotting graphs using Origin 2023 [71] for the NMC811 precursor by comparing obtained diffractogram with reference patterns, crystallographic open database (COD) [72] and international centre for diffraction data (ICDD) database [73].

Figure 25: PANalytical X`pert Pro MPD Alpha 1 – RAMI

3.3 Structure of precursor studied using PANalytical X`pert Pro MPD powder - RAMI

This technique of a high-temperature *in-situ* XRD (HT-XRD) instrument as shown in Fig. 26a (by, Malvern PANalytical) is used to explore how phase changes in precursor during temperature increasing from 25^{o}C to 900^{o}C. With the Pixel 1D detector and high-temperature stage, the X'pert Pro MPD powder can quickly measure (usually in less than 20 minutes) for the determination of crystal structure, phase identification and quantification, crystalline size, and residual stress analysis from room temperature up to 1200°C and the tube is made of copper (Cu). The atomic and molecular composition of a crystalline substance can be determined using this effective analytical approach. HT-XRD is performed in a specific heating chamber or furnace that can reach high temperatures in a controlled environment. For this study, the following setting was used, start angle = 10°, end angle = 70°, min step size 2θ: 0.001°; Goniometer - PW3050/60 (θ / θ) and sample stage - AP HTK-1200N oven; and overall duration including heating and cooling of testing approximately hours.

In this case, the sample is put on a high-temperature ranging from 25°C to 900°C with precise temperature control, heating rate is 10°C/min. The temperature starts from 25°C, then stepwise increased to 90, 140°C, 190°C, 240°C, 290°C, 340°C, 390°C, 440°C, 490°C, 600°C, 700°C, 800°C, 900°C. It is held at each of these temperature values for 5 minutes before a 30-minute waiting period, after which the temperature is increased further.

Finally, the sample is cooled down to 25°C, as illustrated in Fig. 26b. The overall time for completing the XRD measurement was close to about 16 h.

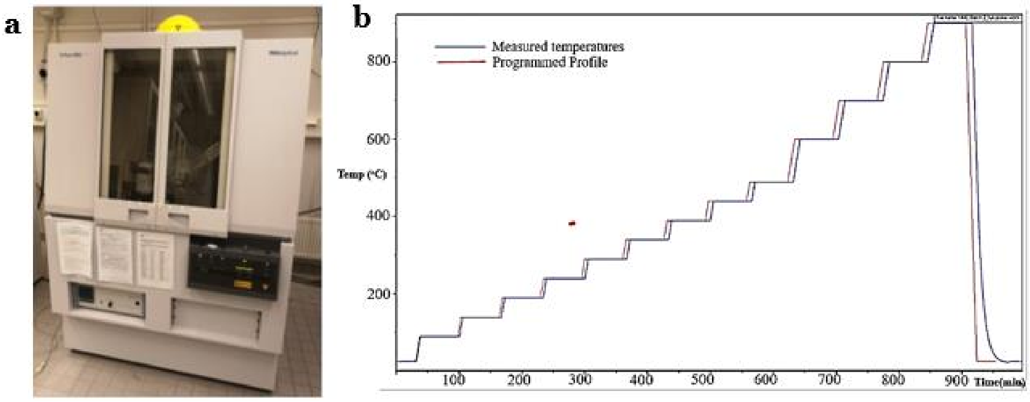

Figure 26: a. PANalytical X`pert Pro MPD powder – RAMI; b. XRD data input profile

3.4 Secondary peaks analyzed using Rigaku SmartLab X-ray diffractometer

The XRD machine as shown in Fig. 27, is an effective instrument for examining the crystal structure, phase identification, and physical properties of materials due to its adaptability, and precision features. Core attributes-3 kW sealed X-ray tube, CBO optics, D/teX Ultra 250 silicon strip detector, core options-PhotonMax high-flux 9 kW rotating anode X-ray source, in-plane arm (5-axis goniometer), HyPix-3000 high energy resolution 2D HPAD detector, Johansson Kα1 optics [74]. The sample types it can handle include powders, thin films, and bulk materials. This XRD is able to provide higher resolution and lower noise signals, smaller peaks can be detected better than PANalytical XRD. The settings that were used for detecting the 0.5% and below mix of MoO_3 with the precursor (the reason will be introduced more detail in results and discussion section). The settings are as follow: Tube voltage – 45 kV; Tube current – 150 mA; Start angle – 10°; End angle – 90°. Scan axis – θ/2θ, Mode - continuous, Range – absolute, Speed duration time – 3 sec. And the manual slits for the incident and detector side can be chosen as per the guidance from the lab expert (Soller (deg)-5, IS L (mm)- 10), Data acquisition mode – 1D, Detector setting – HyPix-3000H.

Figure 27: Rigaku SmartLab X-ray diffractometer [77]

3.5 Sample preparation and testing method for Renishaw Raman spectroscopy

To ensure the safety of the samples, laser settings, and power levels underwent thorough testing across multiple cycles at various points. The goal was to optimize the laser settings for the precursor materials, ensuring reliable experimentation outcomes.

The instrument used for the Raman analysis is from Renishaw company as shown in Fig. 28. A rectangular plate made of glass was used to hold the sample for this test. The sample is placed on the holder. After the Raman instrument has been adjusted for accuracy, the settings are chosen based on the type of sample and information from published sources. The parameters for the experiments are laser power = 1%, accumulation = 5 and 20 (in some cases), exposure time = 1/sec, laser = 532 nm, grating = 830 I/mm, objective = 20 x, 50 x(in some cases), and spectrum range = low to high from 99 to 3666. The reason for the selected values is explained in the results and discussion section. Using these parameters and after adjusting the instrument, the sample is carefully examined using different objective settings. Then, measurements are taken to make sure the desired Raman signals are received.

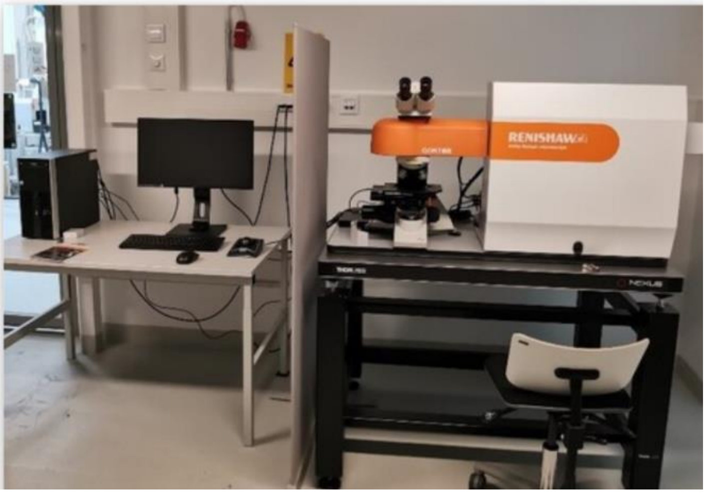

Figure 28: Renishaw inVia™ confocal Raman microscope

Understanding the WiRE software setting, and configuration as shown in Fig. 29, as well as the modes available to conduct experiments for the precursor was crucial to comprehending the capabilities of doing analysis linked to Raman spectroscopy. This section is discussed here to highlight the significance of choosing the parameters, and how they became significant when the sample was tested.

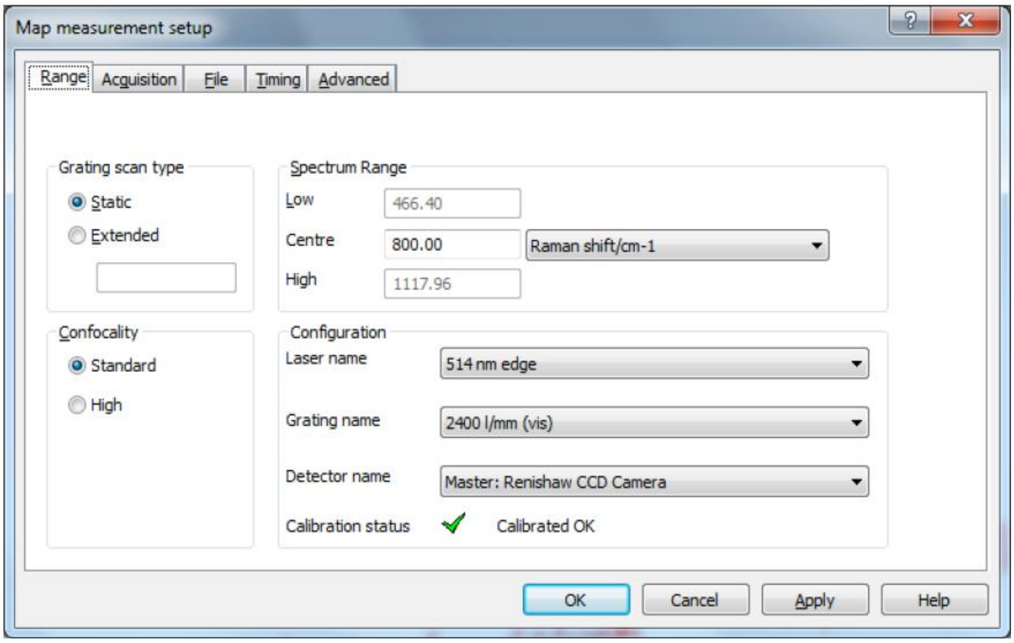

Figure 29: Range tab from WiRE software [75]

- **Grating scan type:** There are 2 types, static and extended. Depending on the wavelength and the grating being used, static extends from 200 cm^{-1} to 500 cm^{-1} on either side of the centre. The spectrum range options can be used to input the desired centre value. The static scan is quicker than the extended scan as it only covers a small area. When a static scan is unable to cover the necessary wavenumber range, extended (synchro scan) scanning is utilized. It scans between the top and lower boundaries entered in the spectrum range.

- **Configuration:** It allows the user to select the type of laser suited for different samples, grating, and detector to be used. And value can vary based on the settings of the instrument, in this case, it was: 532 nm (green) and 785 nm (near infrared (NIR)). The grating can also be selected for this instrument; as default: 1800 I/mm grating for 785 nm laser and 2400 I/mm and 830 I/mm for 532 nm laser.
- **Confocality:** Using the confocality box, a user can choose between high and standard confocal performance. The confocality determines the sample volume from which the signal is obtained. The total Raman signal is also diminished by lowering this volume and raising the spatial resolution while selecting the high confocality option.

It's critical that one initially understands these settings when utilizing Raman spectroscopy to determine how they may affect the sample's Raman scattering and whether the signal agrees with published data. The inferences and assumptions can go in the wrong way if these settings are not handled correctly in Fig. 30.

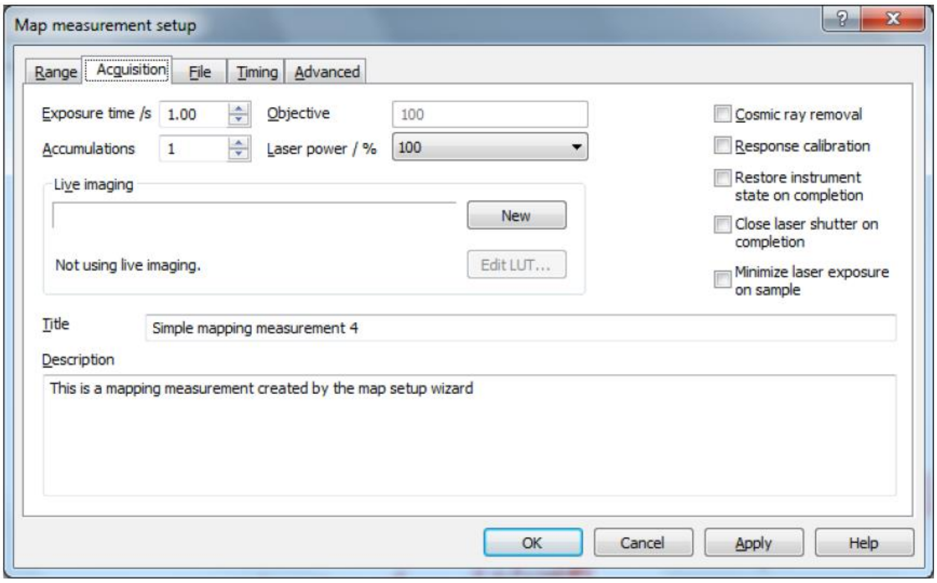

Figure 30: Acquisition tab from WiRE software [75]

- **Exposure time:** The Raman signal is exposed to the detector for the specified amount of time or exposure period. Better spectral signal-to-noise ratios are produced by longer exposure durations. A static grating scan requires a minimum exposure period of 0.02 s.

- **Accumulation:** It represents the number of scan iterations. The automatic co-adding of the accumulations results in spectra with higher signal-to-noise ratios.
- **Laser power:** It is the amount of the maximum laser power that will be employed for a scan. Depending on the laser being used, higher power will improve the signal-to-noise ratio but may also harm some samples.

While testing the sample, the settings for each of these factors are equally crucial. Few trial-and-error tests will help to determine the proper settings because there is limited information in the literature on the best settings for each type of sample.

4. Results and Discussion

This section explains the outcomes of the XRD and Raman spectroscopy tests performed on the samples. The primary goal of this section is to highlight the findings and major lessons learned from this work while also highlighting the paucity of relevant literature and research efforts to gather such information, which might significantly improve the understanding link between precursor and cathode materials.

4.1 Analysis of NMC811(OH)$_2$ precursor using XRD

The analysis pertains to the measurements of the precursor taken at various time intervals. Just to optimize the program for precursor as shown in Fig. 31 a demonstrates that when the time duration increases, the peaks become more distinct and exhibit lower levels of noise when tested for 1 h and 2 h. The diffractogram that was acquired displays a peak that is in closest proximity to the reference pattern of $Ni(OH)_2$. The peaks were indexed to hexagonal $Ni(OH)_2$ crystal structure (ICDD:04-012-5845) with lattice cell parameters a=b= 3.1140 Å, and c= 4.6170 Å. Overall, there are 9 peaks visible for this precursor for the axis range from 10° to 90°. The diffraction peaks are visible at the peak position and corresponding planes as shown in Table 2.

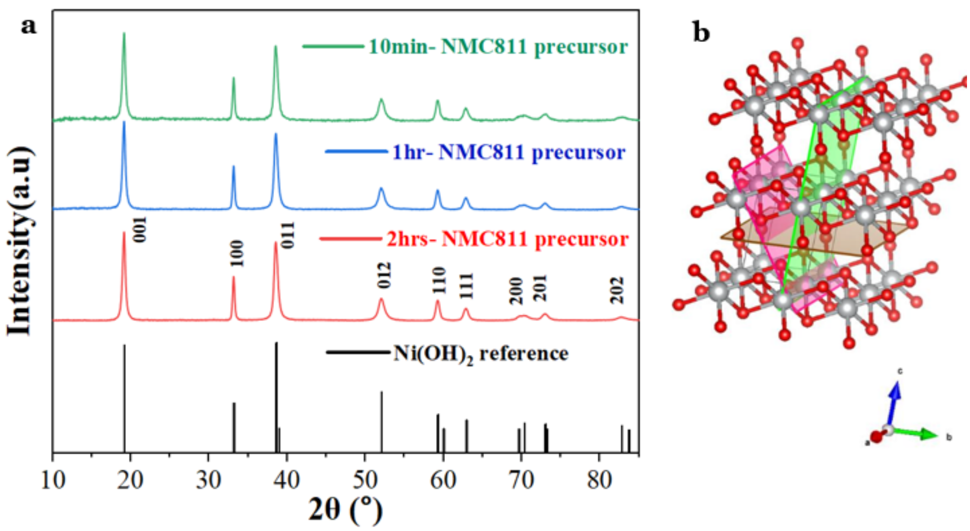

Figure 31: a. XRD patterns for P-NMC811; b. Crystal structure of $Ni(OH)_2$, the green lattice plane is (010), brown is (001), the pink is (011)

Table 2: P-NMC811 peak position and plane measured using XRD for 1h

Peak position (°)	19.1	33.0	38.4	51.9	59.2	62.0	69.7	73.1	82.7
Crystal planes	(001)	(100)	(011)	(012)	(110)	(111)	(200)	(201)	(202)
Peak intensity	1301	928	2000	667	461	294	126	154	88

The (001) lattice plane is the highest peak at 2θ angle of 19.13°. The precursor sample displays good crystallinity, which is evident from the pointed peaks it exhibits, and it is similar to the peak from the literature reviewed [54]. Additionally, the crystal structure of $Ni(OH)_2$ is presented in Fig. 31b to indicate the potential crystal planes.

Based on these results, all trials for this precursor are conducted for one hour because there is little change from the 2 hrs plot all peaks are apparent and there is less noise. And because all of the peaks are visible in this range, the axis angles are set for the range of 10° to 85°.

4.2 Analysis of NMC811$(OH)_2$ precursor using *in-situ* high-temperature XRD (HT-XRD)

An XRD experiment conducted at high temperatures revealed significant phase changes in the structure of the P-NMC811. The detail of program introduced in section 3.2. First, from 25°C to 240°C, the XRD diffraction pattern displayed characteristic peaks that corresponded to the P-NMC811 as also shown in the previous result in Fig. 31. However, upon heating, noticeable shifts in the peak positions and changes in their intensity were observed, indicating thermal expansion, lattice distortion, and also phase change is happening, and the water content vanishes at temperature between 190°C and 240°C [57]. Additionally, the appearance of new diffraction peaks after 190°C suggested potential phase transitions or the formation of secondary phases [57].

The observed structural changes can be attributed to several factors, including the thermal decomposition of precursor species, rearrangement of metal cations within the crystal lattice, and diffusion processes. From Fig. 32 a, a few observations include the peak at (011) plane split to form new peaks at 240°C and peaks at plains (012) and (110) at 2θ angle of 50° and 60° disappears.

Additionally, the peak data at 25°C before and after the XRD test show that heating the precursor sample permanently altered the structure. The same inference may be made from Fig. 32.b, where the scenario is presented intriguingly by the heatwave. Up until 190°C, it can be observed that the intensity is declining; however, once the bonds start to break at 240°C, it is then possible to see that the intensity is growing and that the plot is shifting to the left as the temperature rises, demonstrating formation of oxides.

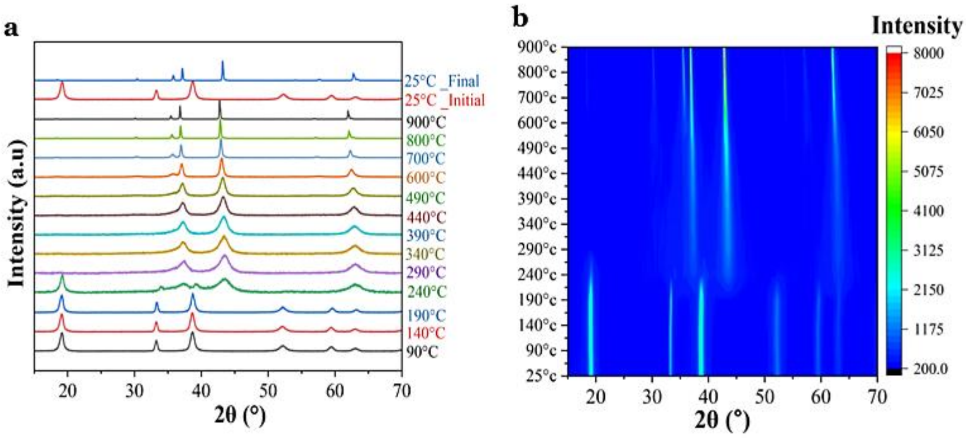

Figure 32: a. *In-situ* HT-XRD of P-NMC811; b. Heatwave plot of P-NMC811

To analyze what type of bonding is formed during this temperature range, the data was analyzed using HighScore software [76] to check the peaks match with various compounds and structures. The XRD patterns from the analysis at temperatures of 240°C, 290°C, and 900°C, and a comparison between 900°C and 25°C final temperature, are shown in Fig. 33. These temperatures were chosen because they fall within a range where the precursor's structural alteration is more pronounced. In Fig. 33 a, at 240°C, some peaks still match $Ni(OH)_2$, indicating the presence of the hydroxide form of Ni is still intact. At the same time, some peaks match oxides of manganese, cobalt, and nickel (NiO, ICDD: 00-001-1239; CoO, ICDD: 04-005-4395; MnO_2, ICDD: 00-044-0992) indicating that hydroxide started breaking down to form its oxides. It's also noteworthy to observe that at 290°C as shown in Fig. 33 b, the peaks correspond to Ni, Mn, and Co oxides (NiO, ICDD: 00-001-1239, MnO, ICDD: 04-006-0700, CoO, ICDD: 04-005-4395), no $Ni(OH)_2$ peaks left at 290°C. Then, in Fig. 32 c, at 900°C, the peak of the precursor is matching with the corresponding peaks of MnO, CoO, NiO, and some additional peaks that belong to Mn_3O_4, Co_3O_4 (Co_3O_4, ICDD: 04-022-8335, Mn_3O_4, ICDD: 00-013-0162). Noticeably the precursor peaks are sharper as they complete the formation of oxide compound from the hydroxide form and are more crystalline compared to how it was at 240°C and 290°C. Additionally in Fig. 32 d, the peak at 25°C is displaced to the right even though the strength and peak generated remain the same once the temperature was reduced from 900°C to 25°C. Thus, it can be concluded that the precursor structure from hydroxide has transformed to its oxide forms during this progress.

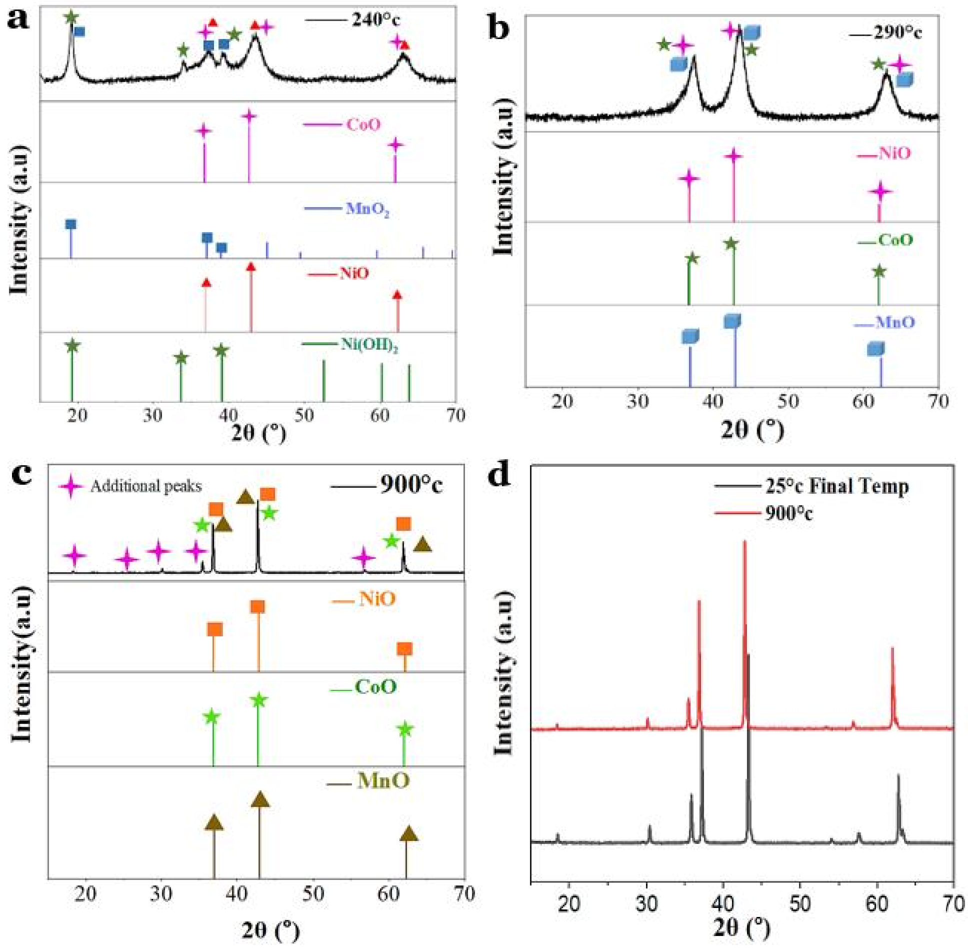

Figure 33: *In-situ* HT-XRD of P-NMC811 a. at 240°C; b. at 290°C; c. at 900°C; d. comparison at 900°C and at final temp of 25°C

4.3 XRD analysis of NMC811(OH)$_2$ precursor mixed with MoO$_3$

To analyze the use of the compound MoO_3 first the XRD test was conducted using only MoO_3 as shown in Fig. 34 a. After which the sample P-NMC811 mixed with MoO_3 by 0.5 by wt.% was tested using the PANalytical XRD, no peaks were visible, after which the sample quantity the precursor mixed with MoO_3 was increased to 1 wt %. While tested for XRD many new peaks started to appear, as shown in the Fig. 34 b. The diffraction peaks of MoO_3 (in Fig. 34 a), along with their corresponding positions and planes, are detailed in the Table 3 below.

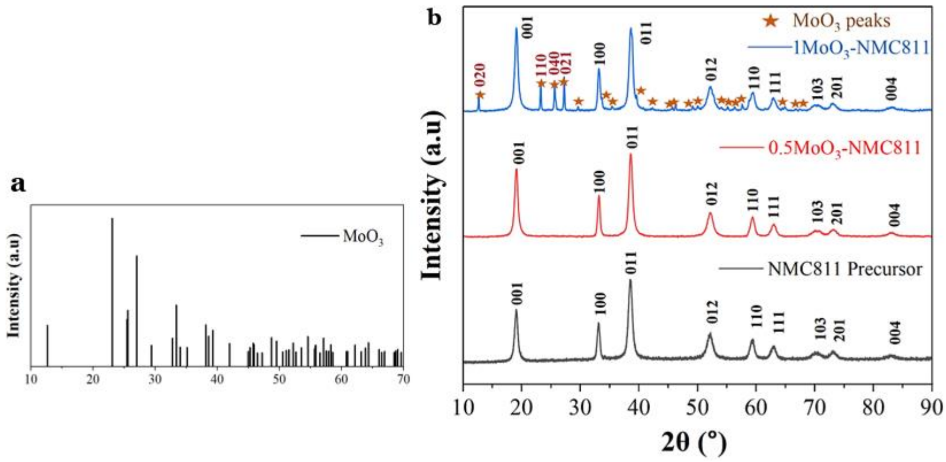

Figure 34: MoO_3 peak obtained from lab XRD; b. XRD spectrum of P-NMC811 mixed with MoO_3

Table 3: The peak angles and peak planes of P-NMC811 mixed with MoO_3

Peak position	12.67°	23.24°	25.61°	27.23°
Peak planes	(020)	(110)	(040)	(021)
Peak intensity	408	651	661	755

This result suggests that the relative abundance of different phases in the P-NMC811 in combination with MoO_3 (1 %) can also be estimated using XRD. One can observe changes in the placement of the diffraction peaks, changes in the intensities of the peaks, or the development of new diffraction peaks corresponding to new phases. This test was done to reveal whether the crystal structure of P-NMC811 or MoO_3 has changed due to contact or solid-state processes. Also, if there are impurities or unexpected phases in the P-NMC811 in combination with MoO_3 can be recognized and identified by carefully studying the diffraction pattern. In this case, since the mixture is prepared by hand mixing and tested, there are no new additional phases other than that of precursor and MoO_3. The main idea here was to understand how much percent of the MoO_3 can be detected using PANalytical XRD, and it is clear that the amount required was more than 0.5% by weight.

The results obtained when the same 0.5% by weight MoO_3 was evaluated using the Rigaku SmartLab X-ray diffractometer (HR-XRD) are shown in Fig. 35. When the XRD used has a greater resolution, the background noise decreases and some of the peaks become more noticeable. Hence to detect smaller peaks for future work, it is also a good idea to examine whether the data can be processed with a higher power and resolution XRD to increase detection limitation.

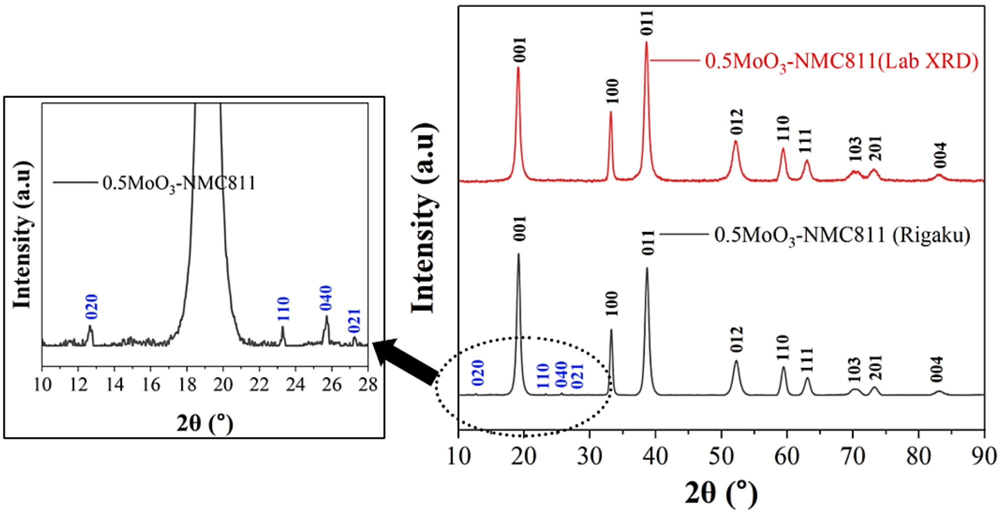

Figure 35: Comparison of P-NMC811 mixed with MoO_3 using different XRD

4.4 XRD analysis of NMC811$(OH)_2$ precursor mixed with $Al(OH)_3$

When detected $Al(OH)_3$ with precursors by using XRD, as shown in Fig. 36, the findings were made similar to those for MoO_3. According to the data, $Al(OH)_3$'s secondary peaks are still discernible when mixed with 0.25% of its weight. The data was also tested for 0.1%, but no secondary peaks could be seen, thus it was not included. The peak intensity is not as intense for $Al(OH)_3$ as it is for MoO_3. Three peaks of $Al(OH)_3$ can be seen visible close to 2θ value of 20°, which are at 18.28°, 20.28°, 20.52°, and the peak height corresponding to these are 1000, 349.2 and 172. So, the one that has the maximum peak height is 18.28°, which corresponds to the (002) plane. The P-NMC811 has a peak at 19.13°, which corresponds to the plane (001), which can be considered very close to the value of the highest peak of $Al(OH)_3$ as shown in Table 4.

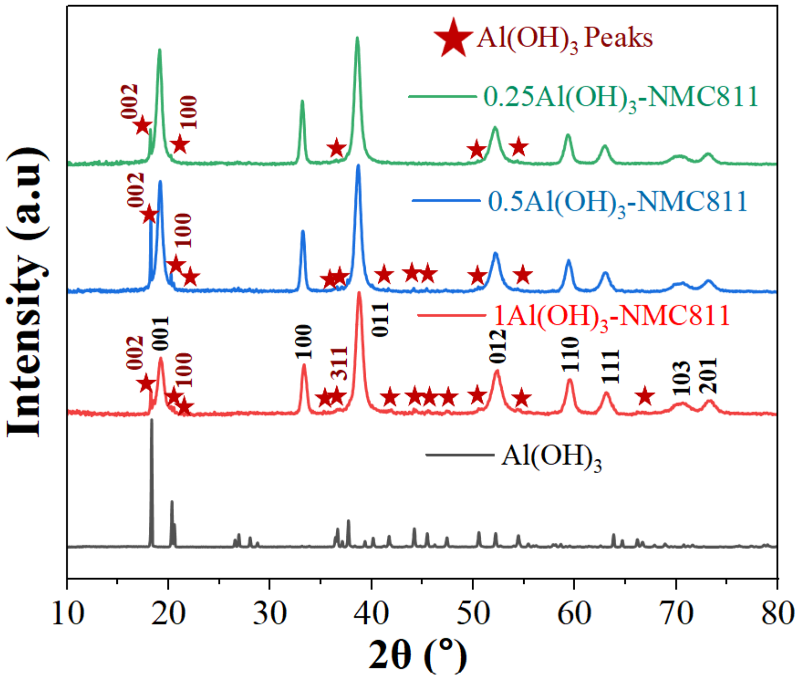

Figure 36: XRD spectrum of P-NMC811 mixed with $Al(OH)_3$

Table 4: The peak angles and peak planes of P-NMC811 mixed with $Al(OH)_3$

Peak position	18.28°	20.28°	20.52°
Peak plane	(002)	(100)	(110)
Peak intensity	1000	349	172

When $Mg(OH)_2$, was tested, the peaks were similar to this P-NMC811, therefore it was difficult to locate the peaks as shown in Fig. 37. Even though some small peaks can be seen visible (103), and (004) lattice parameter. In some circumstances, peaks can overlap, and as a result, the individual peaks may not be distinguishable. Thus, further measurement is not for Mg(OH)2 compound.

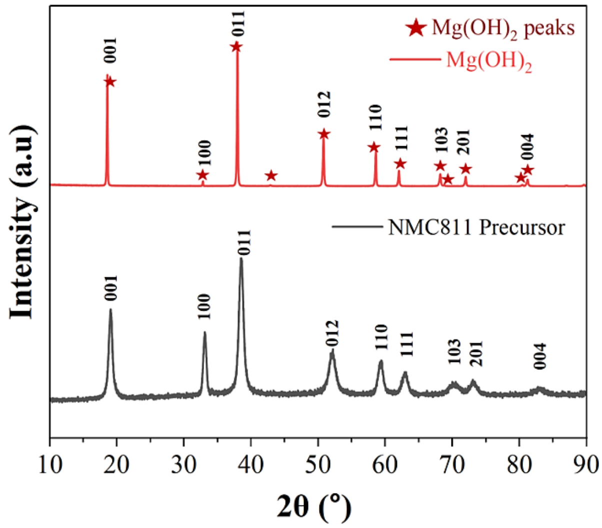

Figure 37: XRD spectrum comparison of P-NMC811 and $Mg(OH)_2$

4.5 XRD analysis of NMC811$(OH)_2$ precursor mixed with $Zr(OH)_4$

The P-NMC811 combined with $Zr(OH)_4$ underwent an XRD examination. The main purpose of the analysis of the findings was to determine how much $Zr(OH)_4$ mixture would be detectable of the secondary peaks from the P-NMC811 peaks. When $Zr(OH)_4$ peaks as depicted in Fig. 38 a, it is evident that the peak's intensity and amorphous peak pattern are very different from the crisp, highly crystalline peak pattern of the P-NMC811. To determine whether the peak could be seen when evaluated using XRD, the mixture was therefore added at a larger percentage (5%, 50% by weight). The results are displayed in Fig. 38 b. The findings make it abundantly clear that even with an addition of 50% by weight, which is never a realistic possibility, zirconium hydroxide's amorphous peak height cannot be traced by XRD, due to amorphous phase property.

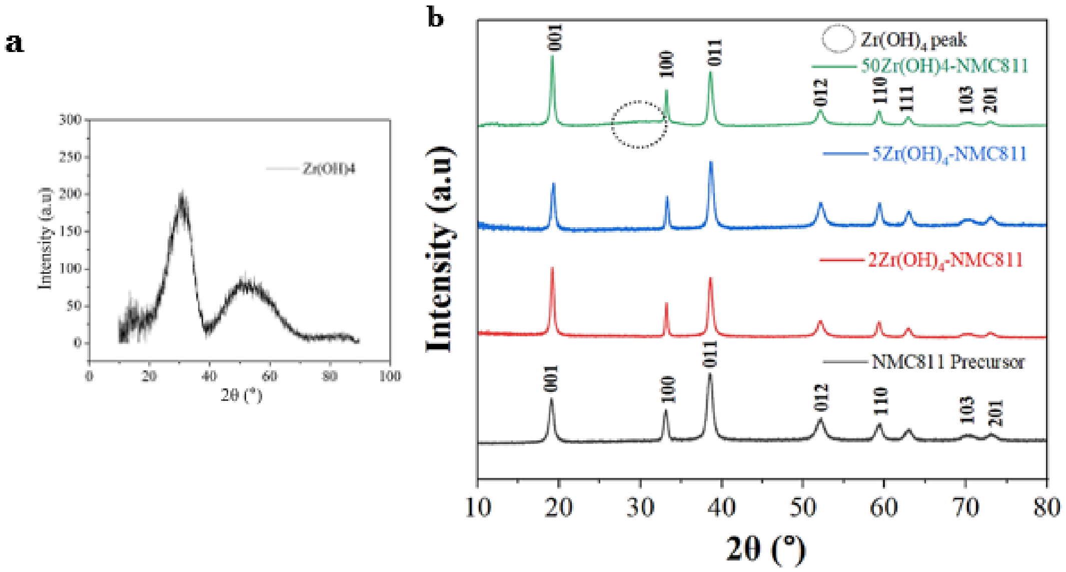

Figure 38 a. XRD peak of $Zr(OH)_4$; b. P-NMC811 mixed with $Zr(OH)_4$

4.6 Raman spectroscopic analysis of $NMC811(OH)_2$ precursor

In the initial stages of the Raman spectroscopic assessment, the importance of laser power was examined to see how the sample would behave at increasing power output. The QONTOR inVia confocal microscope from Renishaw [77] is used for all the testing of samples, and the specifications suggest that this microscope has excellent special resolution, close to a maximum of 1 μm. Table 5 provides an actual representation of how laser power may affect the powder-like sample P-NMC811. To observe the change in Raman shift, a different laser intensity was given to the same sample point in Table 5. The x and y axis of the shift may not be apparent in this image since it simply serves to highlight how the overall shape of the plot varies with power; a more thorough representation is given in the results that follow. It is evident that when the laser power is too low, there is a lot of Raman shift noise; however, when the power is increased by 1%, the shifts become clearer, and the Raman peaks are now clearly identifiable. When evaluated at 5%, shifts can then be shown to get sharper and peaks to become more obvious. When the laser power was increased to 10%, a different result was obtained. After the test was completed, it became evident that the sample's original point of focus had disappeared, and some of the peaks themselves were no longer visible and had altered their output. This observation indicates a variation in the precursor sample due to changes in laser power percentage.

Table 5: Raman shift for different laser power

Laser Power (%)	Image before testing	Image after testing	Raman shift
0.5	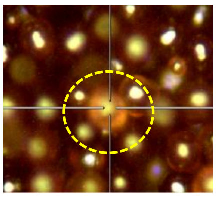	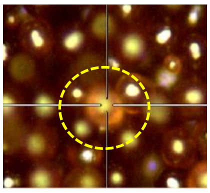	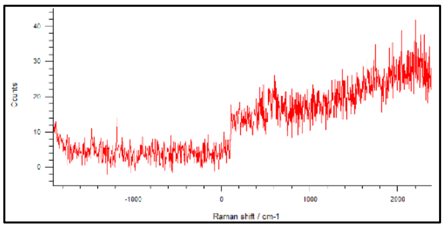
1	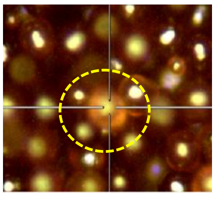	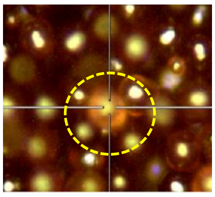	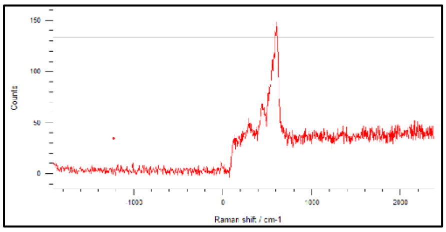
5	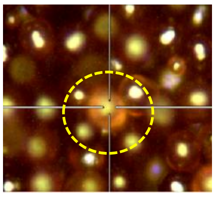	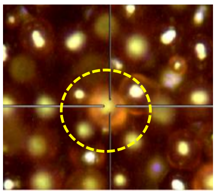	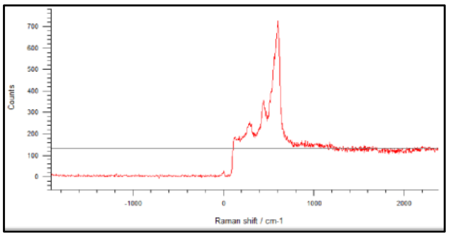
10	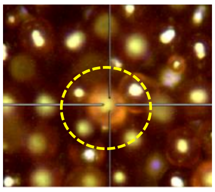	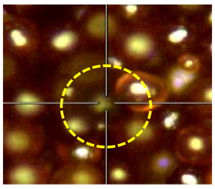	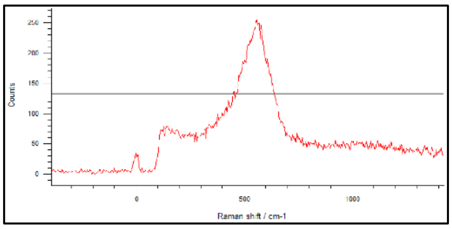

After this outcome, it is still important to test the laser power at various particle sizes to determine whether the material will be affected by the greater laser power. The sample was tested for laser power at 1% and 5% since it is a more suitable condition to obtain detailed information. The outcomes showed that, at 1% laser power across the board for all particle sizes, the material remained stable, and Raman spectra were visible, but at 5% power at specific particle size points are not stable, as shown in Table 6.

Table 6: Raman images at laser power 5%

Image before testing	Image after testing	Raman shift
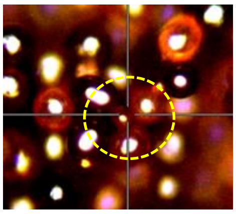	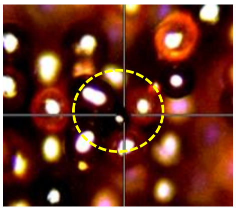	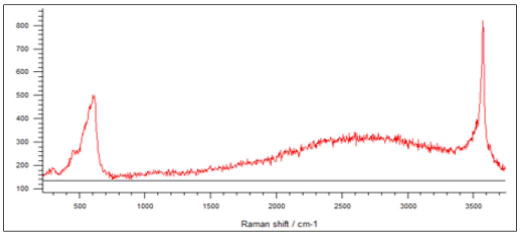
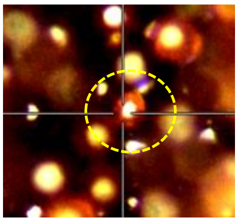	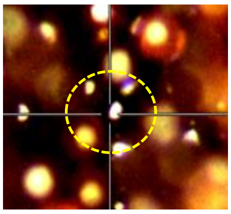	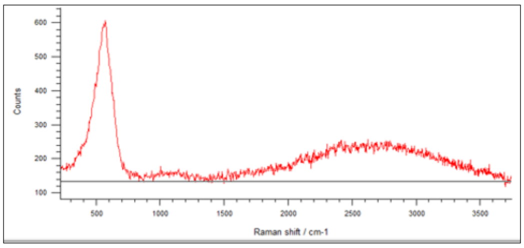
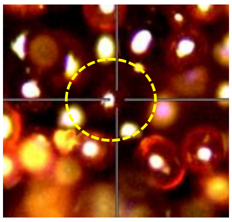	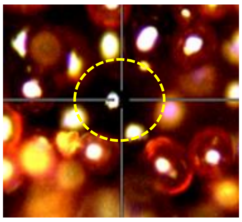	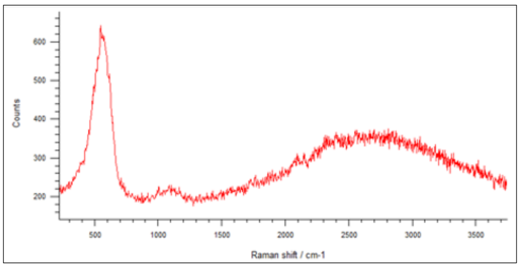

After optimized measurement parameters. Raman spectra from various crystal phases may be distinctive, enabling identification and characterization. Raman peaks that are distinctive to various functional groups and crystal structures allow for the identification of the precursor's chemical nature and structure. So, for obtaining the Ramen spectrum for the P-NMC811 various references were scrutinized to understand the spectrum range and information.

The Raman spectra for P-NMC811 were collected using a 532 nm laser line at the grating of 830 I/mm, laser power of 1%, exposure time 1/sec, accumulation 50, and spectra range between a low and high value of 97 to 3666 Raman shift/cm^{-1} as shown in Fig. 39 b, more detail from 350 to 800 Raman shift/cm^{-1} is shown in Fig. 39 a.

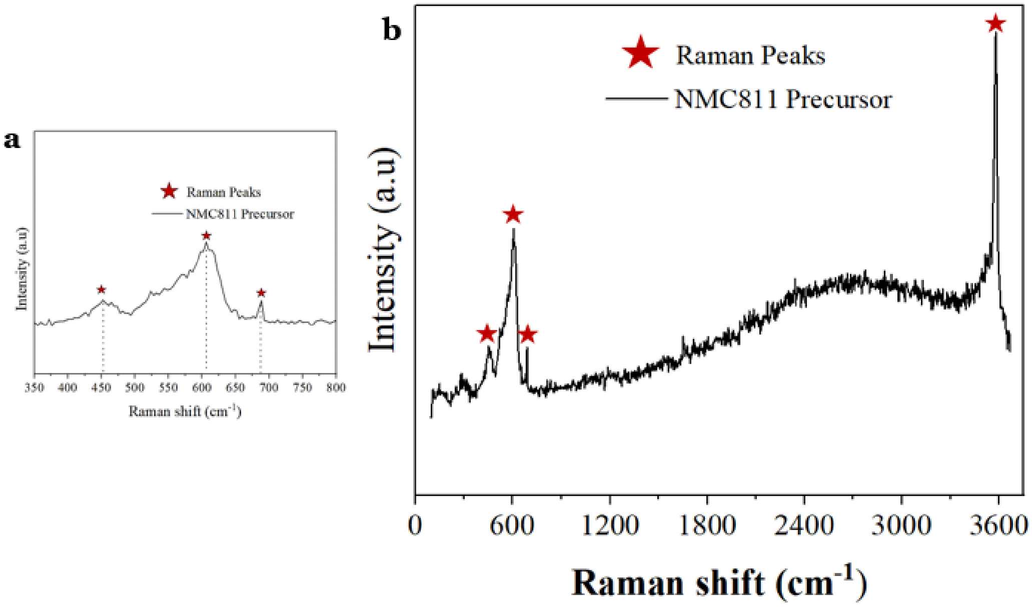

Figure 39: a. Raman spectra of P-NMC811 peak enlarged between 350 and 800 cm^{-1}; b. Raman spectra of P-NMC811

For analysis, various literature was referred [78] [79] as the information available was quite limited regarding the Raman spectrum for P-NMC811. According to the examination of the plots in Fig. 39, the vibrational modes of Ni-O(H) are represented by the peak at 452 cm^{-1} [80], and Mn and Co oxide groups are represented by the peaks between 610 and 680 cm^{-1}, respectively as marked in Fig. 39 a [81]. Additionally, the OH group is represented by the peak that is visible at a range of 3600 cm^{-1} [82]. Here, different spots were measured, and the results are reproducible and repeatable. These findings imply that Raman spectroscopy can generate signals from these precursors, and it is also apparent that the precursor required suitable laser power which was limited investigated by others before.

4.7 Raman spectroscopic analysis of NMC811(OH)$_2$ precursor mixed with MoO_3

The findings of the Raman spectroscopic study of MoO_3 combined with P-NMC811 are shown in Fig. 40. The peaks of MoO_3 can be found using Raman spectroscopy. It's fascinating to observe that the peaks become more apparent as the combination percentage by weight of the compound was increased with the precursor. Fewer peaks are seen when the compound is blended at 0.5% by weight. And when tested for even smaller quantities like 0.25% and below there were no peaks available, because of which it was not added to the result plots. The MoO_3 peaks match for Raman signals compared to XRD data when the percentage is increased to 1%. Even though there is limited literature to support these findings, the analysis may still be stated to be rational since, as can be seen on the MoO_3 plot in red, the OH-Raman peak is not present when tested while all other peaks contain the presence of an OH group that is a part of the precursor, and MoO_3 peaks can be seen distinctive to the precursors peaks, which are in the star and square symbols. Also, it can be observed the Raman shift of MoO_3 is closer to the P-NMC811 peaks of the precursor. These results demonstrate that Raman spectroscopy is a promising method to detect the precursor of secondary compounds' functional group present while added to precursors.

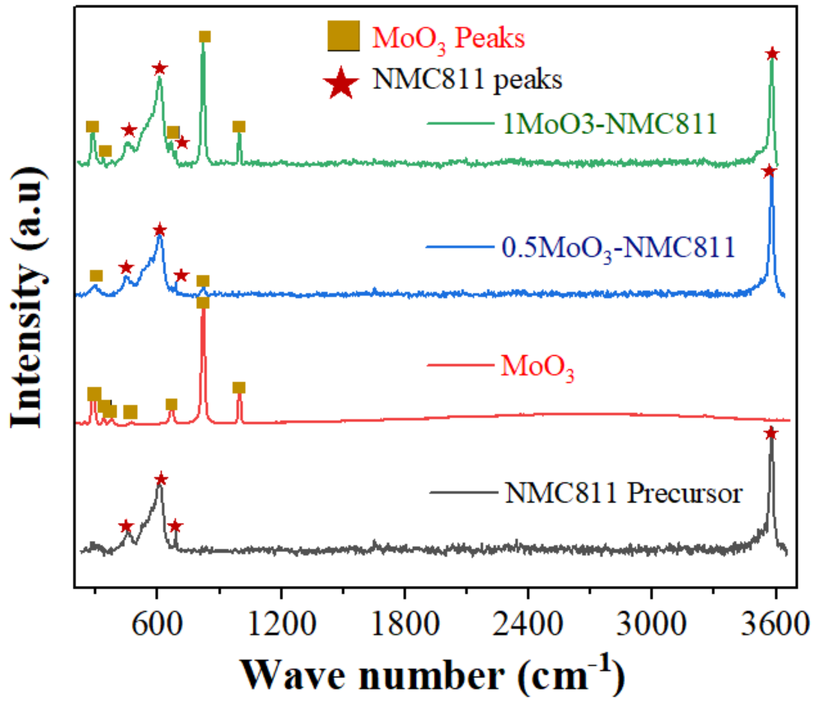

Figure 40: Raman spectroscopic analysis of P-NMC811 mixed with MoO_3

4.8 Raman spectroscopic analysis of $NMC811(OH)_2$ precursor mixed with $Al(OH)_3$

The Raman spectroscopic analysis was conducted with an optimized parameter setting. The result obtained as in Fig. 41 implies the absence of Raman shift for the $Al(OH)_3$. The test was conducted for different percentage of the sample as shown before in Table 1, since there was no difference in the Raman spectroscopy only 2 of the mixed plot is shown below. The sample was tested for different particle sizes and tried to be analyzed with different grating options still the secondary signals were not detectable.

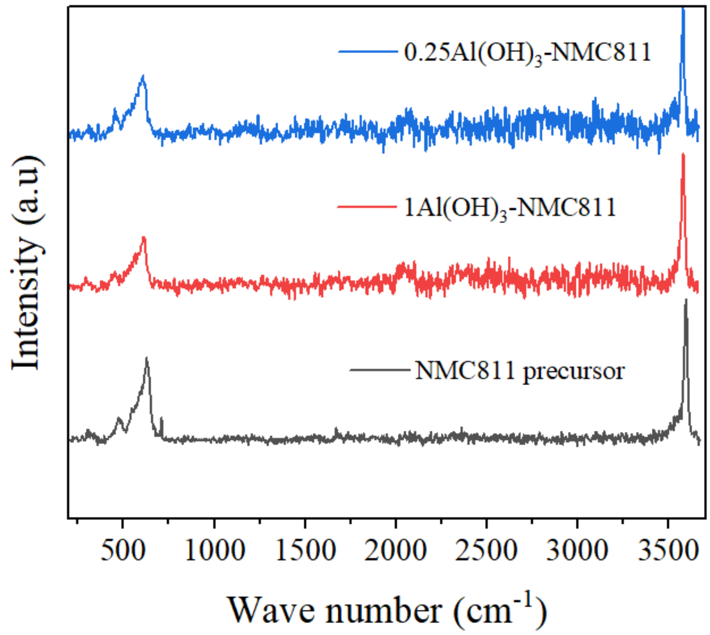

Figure 41: Raman spectroscopic analysis of P-NMC811 mixed with $Al(OH)_3$

Thus, to understand further various literature study was conducted to study the Raman shift for $Al(OH)_3$. According to the study, it was difficult to produce the spectrum even after numerous failed attempts. However, these works on literature still contain some Raman shifts, albeit the range is very different [84] [85]. So, to do a more thorough analysis, I attempted testing with various settings while solely using $Al(OH)_3$ to check the peaks as shown in Fig. 42. As can be seen at a higher laser power of 5% and 10%, a short Raman shift close to 600 cm^{-1} which is close to the peak from reference [83]. But at 1% laser power, the peak is very minimal which is not enough to be seen when added to NMC811 precursor. Based on these results, $Al(OH)_3$ mixed with NMC precursor is not suitable for detecting the secondary peaks using Raman spectroscopy. One explanation for this phenomenon could be that MoO_3 has a more complex molecular structure compared to $Al(OH)_3$. Raman spectroscopy is sensitive to the vibrational modes of molecules within a material. Since MoO_3 has a larger and more intricate molecular structure than $Al(OH)_3$, it may exhibit a greater variety of vibrational modes, increasing the likelihood of detectable Raman signals.

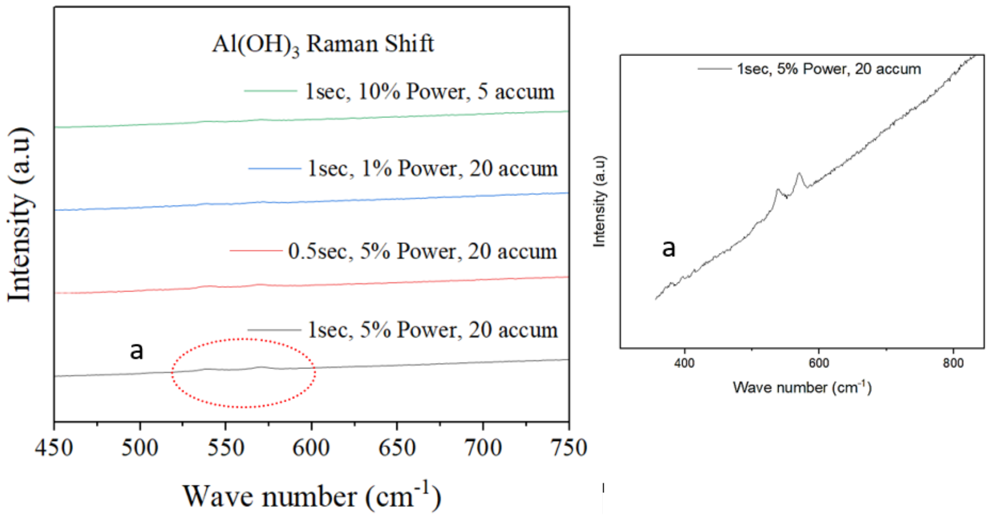

Figure 42: Raman shift for Al(OH)$_3$ at different settings

For Zr(OH)$_4$ and Mg(OH)$_2$, the Raman spectroscopy analysis was not performed. As a result of Zr(OH)$_4$'s amorphous nature, invisible peaks at low concentrations, and undetectable spectra when only Zr(OH)$_4$ was tested using Raman, additional tests were omitted, and since Mg(OH)$_2$'s peak position matched that of the P-NMC811, thus, it was decided not to invest further.

5. Conclusion

In this thesis, an effort was made to comprehend how the NMC811(OH)$_2$ precursor could be detected using XRD and Raman spectroscopy when it was mixed with additional compounds.

The initial experiments were started using PANalytical XRD to detect any secondary phases in the P-NMC811 and were compared to the peaks of Ni(OH)$_2$ (ICDD:04-012-5845). The peaks obtained from the precursor showcased high crystallinity. And for the results from the *in-situ* HT-XRD pattern revealed the conversion of Ni, Mn, and Co hydroxide structures to oxides in a temperature range of 190°C to 900°C. The analysis at 900°C confirmed the presence of crystalline oxide peaks

The additional compound detection testing by XRD was conducted for four compounds, MoO$_3$, Al(OH)$_3$, Zr(OH)$_4$, and Mg(OH)$_2$. The secondary peaks after mixing with the precursor, the addition of compounds at a weighted average addition rate of roughly 1% generally produced the secondary phase detectable results for MoO$_3$ and Al(OH)$_3$ but not for Mg(OH)$_2$, even though Mg(OH)$_2$ showcased high crystalline structure, but the peaks were mostly coinciding with the P-NMC811 peak positions. The samples were tested using higher power instruments like Rigaku XRD the better identification of peaks at 0.5% by weight of MoO$_3$ was possible as explained in the results. For Zr(OH)$_4$ (peaks were weak) the peaks cannot be detected by XRD due to its amorphous phase.

Developed the optimal condition of Raman signal for P-NMC811. Ni, Mn, Co, and OH functional groups were detected using the Raman spectrum. In general, various peaks of compounds were visible in the Raman signals when mixed compounds made up 1% of the sample weight for MoO$_3$. There were few signals when the percentage by weight was less than or equal to 0.5%. Peak strength for MoO$_3$ was higher when compared to Al(OH)$_3$'s spectrum. Additionally, with laser powers greater than 5%, there was only a minor peak from Al(OH)$_3$ that could be seen, which is not good for mixing with the precursor. For Zr(OH)$_4$ and Mg(OH)$_2$, Raman spectroscopy was not investigated as results from XRD were not promising.

In general, the study done for this thesis was very helpful in understanding the precursor material and the detection range when employing XRD and Raman spectroscopy. The characteristics of the precursor can be further investigated using *in-situ* high-temperature XRD analysis, and even though the outcomes of mixing the precursor with compounds cannot be compared directly to actual doping, the detection potential, and settings from this thesis work for XRD and Raman spectroscopy, could be advantageous.

6. Future research prospect

This study proves valuable for future research into functional group identification. However, some compounds, such as $Al(OH)_3$ or $Zr(OH)_4$ powder samples, exhibit weak Raman spectroscopy signals; this could change when these compounds are introduced as a dopant, therefore the potential for using Raman spectroscopy for future investigations cannot be eliminated until further analysis. Also, focused studies can be conducted to better analyze the temperature at which the crystal structure and crystal size change, as well as identify any contaminants in the precursor. As evident from these results, the data obtained provides a foundation for approximating the actual doping strategy. This study may be valuable for considering the potential use of these compounds or others in future experiments as prospective dopants for Ni-rich cathode materials for lithium-ion batteries.

7. Reference

[1] Zhang, Q., Bruck, AM, Stavola, AM, Liang, W., Aurora, P., & Gallaway, JW (2021). Enhanced Electrochemical Stability of Sulfide-Based $LiNi_{0.8}Mn_{0.1}Co_{0.1}O_2$ All-Solid-State Batteries by Ti Surface Doping. Batteries & Supercaps , 4 (3), 529-535.

[2] Steiner, J. D., Cheng, H., Walsh, J., Zhang, Y., Zydlewski, B., Mu, L., ... & Lin, F. (2019). Targeted surface doping with reversible local environment improves oxygen stability at the electrochemical interfaces of nickel-rich cathode materials. ACS applied materials & interfaces, 11(41), 37885-37891

[3] Gao, Y., Park, J., & Liang, X. (2020). Comprehensive study of Al- and Zr-modified $LiNi_{0.8}Mn_{0.1}Co_{0.1}O_2$ through synergy of coating and doping. ACS applied energy materials, 3(9), 8978-8987

[4] Xia, Y., Zheng, J., Wang, C., & Gu, M. (2018). Designing principle for Ni-rich cathode materials with high energy density for practical applications. Nano Energy, 49, 434-452

[5] Dalkilic, M., Schmidt, A., Schladt, TD, Axmann, P., Wohlfahrt-Mehrens, M., & Lindén, M. (2022). W-Doping of Dense NMC811 Hydroxide through Wet-Impregnation and Its Impact on Crystal Structure, Phase Transition Related Gas Evolution and Electrochemical Performance at Elevated Upper Cut-Off Voltage. Journal of The Electrochemical Society , 169 (12), 120501.

[6] Susai, F. A., Kovacheva, D., Chakraborty, A., Kravchuk, T., Ravikumar, R., Talianker, & Aurbach, D. (2019). Improving performance of $LiNi_{0.8}Co_{0.1}Mn_{0.1}O_2$ cathode materials for LIBs by doping with molybdenum-ions: theoretical and experimental studies. ACS applied energy materials, 2(6), 4521-4534.

[7] Li, M., Shan, R., Abdulla, A., Tian, J., & Gao, S. (2023).High energy capacity or high-power rating: Which is the more important performance metric for battery energy storage systems at different penetrations of variable renewables? Journal of Energy Storage, 59, 10656

[8] Liu, C., Neale, Z. G., & Cao, G. (2016). Understanding electrochemical potentials of cathode materials in rechargeable batteries. Materials Today, 19(2), 109-123

[9] Kakade, S. (2021, June 22). Cathode - the energy source of a LIB. Emerging Technology News. https://etn.news/energy-storage/cathode-the-energy-source-of-a-li-ion-battery

[10] Doeff, M. M. (2011). Batteries: overview of battery cathodes.

[11] Shao, L., Zhang, Y., Zheng, X., He, X., Zheng, Y., & Liu, Z. (2023). A Review of Remaining Useful Life Prediction for Energy Storage

Components Based on Stochastic Filtering Methods. Energies, 16(3), 1469.

[12] Tsai, Y. T., Wu, C. Y., & Duh, J. G. (2021). Synthesis of Ni-rich NMC cathode material by redox-assisted deposition method for LIBs. Electrochimica Acta, 381, 138244.

[13] Admin. (2022, July 7). High voltage or low voltage batteries: Energy Storage. Deege Solar.

[14] Deng, S., Sun, Q., Li, M., Adair, K., Yu, C., Li, J. & Sun, X. (2021). Insight into cathode surface to boost the performance of solid-state batteries. Energy Storage Materials, 35, 661-668.

[15] Phattharasupakun, N., Wutthiprom, J., Duangdangchote, S., Sarawutanukul, S., Tomon, C., Duriyasart, F., & Sawangphruk, M. (2021). Core-shell Ni-rich NMC-Nanocarbon cathode from scalable solvent-free mechanofusion for high-performance 18650 Li-ion batteries. Energy Storage Materials, 36, 485-495.

[16] Myung, S. T., Maglia, F., Park, K. J., Yoon, C. S., Lamp, P., Kim, S. J., & Sun, Y. K. (2017). Nickel-rich layered cathode materials for automotive LIBs: achievements and perspectives. ACS Energy Letters, 2(1), 196-223.

[17] Tang, L., Cheng, X., Wu, R., Cao, T., Lu, J., Zhang, Y., & Zhang, Z. (2022). Monitoring the morphology evolution of $LiNi_{0.8}Mn_{0.1}Co_{0.1}O_2$ during high-temperature solid state synthesis via in situ SEM. Journal Of Energy Chemistry, 66, 9-15.

[18] Liu, Z. Y., & Zhu, Z. In Situ Probing Characterization of Ni-Rich Nmc811 Thin Film Prepared by Sol-Gel Method in Different Scanning Probe Microscopy Techniques. Available at SSRN 4096080.

[19] Entwistle, T., Sanchez-Perez, E., Murray, G. J., Anthonisamy, N., & Cussen, S. A. (2022). Co-precipitation synthesis of nickel-rich cathodes for Li-ion batteries. Energy Reports, 8, 67-73

[20] Paulsen, J., Nelis, D., Hu, J., Zhu, L., & Robert, E. (2022). U.S. Patent No. 11,476,461. Washington, DC: U.S. Patent and Trademark Office

[21] Myung, S. T., Maglia, F., Park, K. J., Yoon, C. S., Lamp, P., Kim, S. J., & Sun, Y. K. (2017). Nickel-rich layered cathode materials for automotive LIBs: achievements and perspectives. ACS Energy Letters, 2(1), 196-223.

[22] Kartini, E., Fakhrudin, M., Astuti, W., Sumardi, S., & Mubarok, M. Z. (2022, November). The study of (Ni, Mn, Co) SO4 as raw material for NMC precursor in LIB. In AIP Conference Proceedings (Vol. 2708, No. 1). AIP Publishing

[23] Darjazi, H., Gonzalo, E., Acebedo, B., Cid, R., Zarrabeitia, M., Bonilla, F., ... & Nobili, F. (2022). Improving high-voltage cycling performance of nickel-rich NMC layered oxide cathodes for

rechargeable lithium–ion batteries by Mg and Zr co-doping. Materials Today Sustainability, 20, 100236.

[24] Reid, G., & Julve, J. (2016). Second life batteries as flexible storage for renewable energies. Bundesverband Erneuerbare Energie eV (BEE) .

[25] Tarascon, J. M., & Armand, M. (2001). Issues and challenges facing rechargeable lithium batteries. nature, 414(6861), 359-367.

[26] Cready, E., Lippert, J., Pihl, J., Weinstock, I., & Symons, P. (2003). Technical and economic feasibility of applying used EV batteries in stationary applications (No. SAND2002-4084). Sandia National Lab.(SNL-NM), Albuquerque, NM (United States); Sandia National Lab.(SNL-CA), Livermore, CA (United States.

[27] Chawla, N., Bharti, N., & Singh, S. (2019). Recent advances in non-flammable electrolytes for safer LIBs. Batteries, 5(1), 19

[28] Admin. (2022, July 7). High voltage or low voltage batteries: Energy Storage. Deege Solar.

[29] Cloud, M. (2021, August). What is the energy density of a LIB?

[30] Dragonfly Energy. (2022, December 13). A guide to the 6 main types of lithium batteries

[31] Julien, C. M., Mauger, A., Zaghib, K., & Groult, H. (2014). Comparative issues of cathode materials for Li-ion batteries. Inorganics, 2(1), 132-154

[32] Wang, L., Qiu, J., Wang, X., Chen, L., Cao, G., Wang, J., ... & He, X. (2022). Insights for understanding multiscale degradation of $LiFePO_4$ cathodes. EScience, 2(2), 125-137

[33] Cathode materials of LIB | highlights in science ... (2023, April 14)

[34] Ghatak, K., Kumar, H., Nadimpalli, S., & Datta, D. (2017). Effect of Decreasing Cobalt Content on the Electrochemical Properties and Structural Stability of Li(1-x) Ni(y) Co(z) Al (0.05) O(2) Type Cathode Materials. arXiv preprint arXiv:1704.08413

[35] Kemeny, M., Ondrejka, P., & Mikolasek, M. (2023). Comprehensive Degradation Analysis of NCA Li-Ion Batteries via Methods of Electrochemical Characterisation for Various Stress-Inducing Scenarios. Batteries, 9(1), 33

[36] Tran, N. T. T., Lin, C. A., & Lin, S. K. (2023). Insights into the Structural and Thermodynamic Instability of Ni-Rich NMC Cathode. ACS Sustainable Chemistry & Engineering, 11(18), 6978-6987.

[37] Houache, MS, Yim, CH, Karkar, Z., & Abu-Lebdeh, Y. (2022). On the Current and Future Outlook of Battery Chemistries for Electric Vehicles—Mini Review. Batteries , 8 (7), 70.

[38] Sun, H., & Zhao, K. (2017). Electronic structure and comparative properties of $LiNi_xMn_yCo_zO_2$ cathode materials. The Journal of Physical Chemistry C, 121(11), 6002-6010

[39] Pimenta, V., Sathiya, M., Batuk, D., Abakumov, A. M., Giaume, D., Cassaignon, S., & Tarascon, J. M. (2017). Synthesis of Li-rich NMC: a comprehensive study. Chemistry of Materials, 29(23), 9923-9936

[40] Rare Metal Extraction & Processing (Symposium), In Azimi, G., In Ouchi, T., In Forsberg, K., In Kim, H., In Alam, S., In Baba, A. A., Minerals, Metals and Materials Society. (2021). Rare Metal Technology 2021.

[41] Kirsten Hund et al. (2020) Public documents, Public Documents Search.

[42] Mineral Commodity Summaries 2022 - cobalt - USGS publications warehouse.

[43] Mayyas, A., Moawad, K., Chadly, A., & Alhseinat, E. (2023). Can circular economy and cathode chemistry evolution stabilize the supply chain of Li-ion batteries? The Extractive Industries and Society, 14, 101253.

[44] Lucas Marthaler et al. (2023) Market intelligence report - cobra.

[45] Bobba, S., Carrara, S., Huisman, J., Mathieux, F., & Pavel, C. (2020). Critical raw materials for strategic technologies and sectors in the EU. A Foresight Study.

[46] Borisov, SV, & Podberezskaya, NV (2012). X-ray diffraction analysis: A brief history and achievements of the first century. Journal of Structural Chemistry , 53 , 1-3.

[47] Ali, A., Chiang, Y.W. and Santos, R.M. (2022) X-ray diffraction techniques for mineral characterization: A review for engineers of the fundamentals, applications, and Research Directions, MDPI

[48] Debjani Banerjee (2015). "X-Ray Diffraction (XRD)"

[49] Holder, C. F., & Schaak, R. E. (2019). Tutorial on powder X-ray diffraction for characterizing nanoscale materials. Acs Nano, 13(7), 7359-7365.

[50] Joshua T. Guske, Ph.D. (2021) X-ray diffraction shared experimental facility, MIT MRSEC X-ray Diffraction Facility

[51] "Panalytical Scanning Diffractometer x'pert pro MPD Alpha1. 2023, www.nhm.ac.uk

[52] Wijareni, A. S., Widiyandari, H., Purwanto, A., Arif, A. F., & Mubarok, M. Z. (2022). Morphology and Particle Size of a Synthesized NMC 811 Cathode precursor with Mixed Hydroxide Precipitate and nickel sulfate as nickel sources and comparison of their electrochemical performances in an NMC 811 LIB. Energies, 15(16), 5794

[53] Para, M. L., Alidoost, M., Shiea, M., Boccardo, G., Buffo, A., Barresi, A. A., & Marchisio, D. (2022). A modelling and experimental study on the co-precipitation of $Ni_{0.8}Mn_{0.1}Co_{0.1}(OH)_2$ as precursor for battery cathodes. Chemical Engineering Science, 254, 117634

[54] Para, M. L., Querio, A., Amici, J., Versaci, D., Barresi, A. A., Bodoardo, S., & Marchisio, D. (2023). Electrochemical performance optimization of NMC811 through the structure design of its precursor. Journal of Electroanalytical Chemistry, 117630.

[55] Huang, Y., Wang, Z. X., Li, X. H., Guo, H. J., & Wang, J. X. (2015). Synthesis of $Ni_{0.8}Co_{0.1}Mn_{0.1}(OH)_2$ precursor and electrochemical performance of $LiNi_{0.8}Co_{0.1}Mn_{0.1}O_2$ cathode material for lithium batteries. Transactions of Nonferrous Metals Society of China, 25(7), 2253-2259.

[56] Zhou, F., Zhao, X., van Bommel, A., Rowe, A. W., & Dahn, J. R. (2010). Coprecipitation synthesis of $Ni_xMn_{1-x}(OH)_2$ mixed hydroxides. Chemistry of Materials, 22(3), 1015-1021.

[57] Cho, S. J., Chung, C. C., Podowitz-Thomas, S., & Jones, J. L. (2019). Understanding the lithium deficient $Li_xNi_yMn_zCo_{1-y-z}O_2$ ($x<1$) cathode materials structure. Materials Chemistry and Physics, 228, 32-36.

[58] HORIBA - What is Raman spectroscopy?

[59] Gyakwaa, F. (2020). Application of Raman spectroscopy for the characterisation of synthetic non-metallic inclusions found in Al-killed calcium treated steels.

[60] Edinburgh Instruments Ltd - "What is Raman spectroscopy,”.

[61] “inVia™ InSpect confocal Raman microscope https://www.renishaw.com/en/invia-inspect-confocal-raman-microscope--45378.

[62] Coban, A., & Gungor, H. (2022). The Carbon-Based 3D-Hierarchical Cathode Architecture for Li-Ion Batteries. Arabian Journal for Science and Engineering , 47 (6), 7147-7155.

[63] Beccard, B., Karavadra, S., & Dahal, S. (2022). LIB Manufacturing and Quality Control: Raman spectroscopy, an Analytical Technique of Choice.

[64] T. Rizzuto, (Oct, 2017). Technical Note: Sample Damage in Raman spectroscopy

[65] Savina, A. A., Orlova, E. D., Morozov, A. V., Luchkin, S. Y., & Abakumov, A. M. (2020). Sulfate-Containing Composite Based on Ni-Rich Layered Oxide $LiNi_{0.8}Mn_{0.1}Co_{0.1}O_2$ as High-Performance Cathode Material for Li-ion Batteries. Nanomaterials, 10(12), 2381.

[66] IARC Publications, MOLYBDENUM TRIOXIDE https://publications.iarc.fr/_publications/media/download/4880/ce43d96cce0e7478213638226d429d3a711b1477.pdf.

[67] Wikipedia contributors. (2022). Zirconium(IV) hydroxide.

[68] “Aluminium hydroxide,” https://en.wikipedia.org/wiki/Aluminium_hydroxide.

[69] “Agate mortar with pestle, 150 mm,” https://www.auxilab.es/en/laboratory-equipment/agate-mortar-with-pestle-150-mm/.

[70] “Crystal Impact,” https://www.crystalimpact.com/match/download.htm.

[71] “Installing Origin/OriginPro 2023b,” https://www.originlab.com/getstarted.

[72] “Crystallography Open Database,” http://www.crystallography.net/cod/.

[73] “Powder Diffraction FileTM (PDF®) Search,” https://www.icdd.com/pdfsearch/.

[74] “Automated multipurpose x-ray diffractometer (xrd) with guidance software,” https://www.rigaku.com/products/xrd/smartlab.

[75] “TM002-02-A Introduction to WiRE and System start-up,” https://www.ccmr.cornell.edu/wpcontent/uploads/sites/2/2016/08/Wire4_Training_Modules_Compilation-Part-2.pdf.

[76] “HighScore," https://www.malvernpanalytical.com/en/products/category/software/x-ray-diffraction-software/highscore.

[77] https://www.renishaw.com/en/invia-confocal-raman-microscope--6260.

[78] Hu, L., Yu, Z., Hu, Z., Song, Y., Zhang, F., Zhu, H., & Jiao, S. (2015). Facile synthesis of amorphous $Ni(OH)_2$ for high-performance supercapacitors via electrochemical assembly in a reverse micelle. Electrochimica Acta, 174, 273-281.

[79] Yvon, HJ (2017). Raman spectroscopy for analysis and monitoring. Horiba Jobin Yvon, Rama Appl Note , 1-2

[80] Julien, C. M., Abdel-Ghany, A., Mauger, A., Massot, M., Zaghib, K., Gendron, F., & Ramana, C. (2006, June). $LiNi_{0.33}Mn_{0.33}Co_{0.33}O_2$ Positive Electrode for Rechargeable Lithium Batteries. In ECS Meeting Abstracts (No. 4, p. 210). IOP Publishing.

[81] Post, J. E., McKeown, D. A., & Heaney, P. J. (2020). Raman spectroscopy study of manganese oxides: Tunnel structures. American Mineralogist, 105(8), 1175-1190.

[82] Deabate, S., Fourgeot, F., & Henn, F. (2000). X-ray diffraction and micro-Raman spectroscopy analysis of new nickel hydroxide obtained by electrodialysis. Journal of power sources, 87(1-2), 125-136.

[83] Mindivan, H., Kayali, E. S., & Cimenoglu, H. (2008). Tribological behaviour of squeeze cast aluminum matrix composites. Wear, 265(5-6), 645-654.

[84] Phambu, N. (2003). Characterization of aluminum hydroxide thin film on metallic aluminum powder. Materials Letters, 57(19), 2907-2913.

[85] Sieber, T., Ducke, J., Rietig, A., Langner, T., & Acker, J. (2019). Recovery of Li ($Ni_{0.33}Mn_{0.33}Co_{0.33}$) O_2 from LIB cathodes: Aspects of degradation. Nanomaterials, 9(2), 246